

1 Role of Indian Ocean basin mode in driving the interdecadal 2 variations of summer precipitation over the East Asian monsoon 3 boundary zone

4
5 Jing Wang^{1,*}, Yanju Liu², Fei Cheng^{3,*}, Chengyu Song⁴, Qiaoping Li⁵, Yihui Ding², Xiangde Xu⁶

6 ¹Tianjin Key Laboratory for Oceanic Meteorology, and Tianjin Institute of Meteorological Science, Tianjin, China

7 ²National Climate Center, China Meteorological Administration, Beijing, China

8 ³Ningbo Meteorological Observatory, Ningbo, China

9 ⁴Heilongjiang Climate Centre, Harbin, China

10 ⁵CMA Earth System Modelling and Prediction Centre, Beijing, China

11 ⁶State Key Laboratory of Severe Weather, Chinese Academy of Meteorological Sciences, Beijing, China

12
13 Correspondence: Yanju Liu (liuyan@cmac.gov.cn)

14 * Jing Wang and Fei Cheng contributed equally to this work.

15
16 **Abstract.** Based on long-term observational and reanalysis datasets from 1901 through 2014, this study investigates the
17 characteristics and physical causes of the interdecadal variations in the summer precipitation over the East Asian monsoon
18 boundary zone (EAMBZ). Observational evidence reveals that, similarly to previous studies, the EAMBZ precipitation
19 featured prominent interdecadal fluctuations, e.g., with dry summers during the periods preceding 1927, 1939–1945,
20 1968–1982, and 1998–2010, and wet summers during the periods of 1928–1938, 1946–1967, and 2011 onwards. Further
21 analyses identify that the Indian Ocean basin mode (IOBM) is a significant oceanic forcing responsible for the
22 interdecadal variations of the EAMBZ precipitation, playing an independent and critical modulation role. When the cold
23 phase of the IOBM occurs, an anomalous cyclonic circulation is excited around the northeast corner of the tropical Indian
24 Ocean, which further induces a “north-low–south-high” meridional seesaw pattern over the Northeast China–subtropical
25 western Pacific (SWP) sector. Such seesaw pattern is conducive to the enhanced EAMBZ precipitation through linking
26 favorable environments for the transportation of water vapor from the SWP and the convergence over EAMBZ at
27 interdecadal timescales. For this reason, a physical-empirical model for the EAMBZ precipitation is developed in terms
28 of the IOBM cooling. Despite the fact that the extreme summer EAMBZ precipitation cannot be captured by this model,
29 it can still well capture its interdecadal fluctuations and reflect their steady relationship. The key physical pathway
30 connecting the IOBM cooling with the interdecadal variations of the summer EAMBZ precipitation is supported by the
31 numerical results based on the large ensemble experiment and the Indian Ocean pacemaker experiment. Our findings may
32 provide new insights into the understanding of the causes of the interdecadal variations in the summer EAMBZ
33 precipitation, which may favor the long-term policy decision making for the local hydrometeorological planning.

34 35 1 Introduction

36
37 The monsoonal airflows and mid-latitude westerlies are crucial components of the Asian climate system (Li and Zeng,
38 2002; Ding and Chan, 2005; Wang et al., 2008; Wu et al., 2012; Huang et al., 2015; Wang et al., 2017; Chen et al., 2018;
39 J. Huang et al., 2019). These two subsystems can synergistically induce regional precipitation fluctuations over
40 subtropical and mid-latitude Asia during the Northern Hemisphere late spring (May) and summer (June–July–August;
41 JJA) (Qian et al., 2009; Chen et al., 2021; Song et al., 2022; J. Wang et al., 2022). For example, Song et al. (2022) found
42 that May precipitation over the southeastern extension of the Tibetan Plateau (TP) features notable year-to-year variations,
43 which are physically linked to a unique interplay between the upstream mid-latitude westerlies and the Bay of Bengal

44 summer monsoon.

45

46 During the early stage of the northern summer, however, the mid-latitude westerlies shift poleward to the north of the TP
47 abruptly (Yeh et al., 1959; Schiemann et al., 2009). In this context, westerlies of mid-latitude synoptic disturbance and
48 southerlies of East Asian summer monsoon (EASM) collide with each other frequently over the East Asian monsoon
49 boundary zone (EAMBZ) (Qian et al., 2009; Wang et al., 2017; Chen et al., 2018; J. Huang et al., 2019; Zeng and Zhang,
50 2019; Chen et al., 2021; Q. Wang et al., 2021, 2022, 2023). It is essential to point out that although the EAMBZ domain
51 largely overlaps the Northeast Asian area suggested by Si et al. (2021), the EAMBZ is defined from the perspective of
52 the interaction between the mid-latitude westerly and the EASM [see Fig. 1 in Chen et al. (2021); also see the red box in
53 Fig. 1 and associated description in Sect. 2.5.1], not from a geographical notion. Accordingly, the EAMBZ is a transitional
54 climate zone between the EASM-controlled moist region and the westerly-dominated arid region over central Asia (Chen
55 et al., 2010; Chen et al., 2018, 2021), stretching from the eastern flank of the TP to Mongolia and Northeast China. Notably,
56 EAMBZ is a distinguished region with agrarian economy and animal husbandry, which is largely susceptible to water
57 resource variations (Ou and Qian, 2006; Lu and Jia, 2013). Nevertheless, many studies reported that in the past century,
58 the semi-arid EAMBZ underwent the most profound warming over East Asia, suffering from serious aridification and a
59 high risk of desertification (J. Huang et al., 2017, 2019, 2020). In this regard, EAMBZ is deemed one of the “hotspots”
60 highly sensitive to precipitation fluctuations (Qian et al., 2009; Lu and Jia, 2013; J. Huang et al., 2019). Given that the
61 EAMBZ is of an ecologically fragile environment with water shortage, a deep understanding of the reasons for historical
62 changes in summer EAMBZ precipitation could be a prerequisite for in situ ecological improvement and socioeconomic
63 development.

64

65 Existing studies have well documented physical mechanisms responsible for the interannual variability of summer
66 EAMBZ precipitation, highlighting the external moisture supply pathways, the modulators for the wet-dry condition
67 variations [e.g., the mid-latitude westerlies within the Asian westerly jet, the western North Pacific subtropical high, and
68 the EASM], and the remote modulation roles of large-scale teleconnected modes [e.g., Silk Road pattern/circumglobal
69 teleconnection propagating along the westerly jet and the Eurasian teleconnection] and sea surface temperature (SST)
70 anomaly patterns (Huang et al., 2015; Wang et al., 2017; Chen et al., 2018, 2021; Zhao et al., 2019a, 2019b, 2020; Q.
71 Wang et al., 2021, 2022, 2023). For instance, Q. Wang et al. (2022) suggested that the positive phase of the Eurasian
72 teleconnection is connected with a low pressure anomaly in the lower troposphere in EAMBZ and the Mongolia region,
73 thus favoring enhanced summertime precipitation over EAMBZ; and meanwhile, the circumglobal teleconnection is
74 positively coupled with the EAMBZ precipitation, with ascending motion anomalies over EAMBZ during its positive
75 phase. Chen et al. (2021) established that the circulations (i.e., the mid-latitude westerlies and EASM) and the forcing of
76 SST anomalies (SSTAs) can collectively regulate the summer EAMBZ precipitation variability. The variability of
77 westerlies is largely modulated by the Silk Road pattern and the meridional displacement of the westerly jet; while the
78 EASM variability is mainly modulated by the prior wintertime El Niño-Southern Oscillation. The synchronized effects
79 of EASM and westerlies largely contribute to the rainfall variability in EAMBZ. Note that Chen et al. (2021) also pointed
80 out that the Indian Ocean basin mode (IOBM) is simultaneously correlated with the EASM in boreal summer on the
81 interannual timescale, which may be considered as a salient oceanic modulator for the summer EAMBZ precipitation
82 variability. Nevertheless, they paid little attention to the physical mechanisms of how IOBM regulates the year-to-year
83 EAMBZ precipitation. Moreover, Zhao et al. (2019a) found that the tropical northern Atlantic SSTAs have significant
84 impacts on the August rainfall over the monsoon transitional zone in China through inducing a wavetrain over Eurasia
85 and the western North Pacific anomalous anticyclone.

86

87 Compared with the extensively explored interannual variability of the JJA EAMBZ precipitation, less efforts have been
88 devoted to its interdecadal variability. To understand and predict the summer EAMBZ precipitation, exploring its
89 interdecadal variations and the underlying physical causes are also critical, which is the main focus of the present study.
90 Previous studies suggested that the warm-season precipitation over many Asian areas features interdecadal fluctuations.
91 For example, J. Wang et al. (2022) reported that the late spring (May) southeastern TP underwent wet conditions for
92 1928–1961 and 1989–2003, and experienced dry conditions preceding 1927, 1962–1988, and 2004 onwards. Si and Ding
93 (2016) documented that East Asia experienced dry summers from the early 1920s to the 1940s, ~~as well as~~ while wet
94 summers from the late 1900s to the early 1920s, in the 1950s, and from the 1980s to the 1990s. Piao et al. (2021) found
95 that the decadal-filtered summer precipitation over Northeast Asia underwent a sudden decrease around the late 1990s.
96 The ~~oceanic interdecadal signals~~ interdecadal oceanic forcings for the interdecadal changes of the Asian summer rainfall
97 are also extensively investigated, highlighting the crucial modulation roles of basin-scale SST modes of Atlantic
98 multidecadal oscillation (Si et al., 2021), Pacific decadal oscillation/interdecadal Pacific oscillation (IPO) (Si and Ding,
99 2016), and IOBM (Zhang et al., 2018). Among these interdecadal oceanic forcings, it is essential to emphasize the IOBM,
100 a dominant mode of SST variability in the tropical Indian Ocean (TIO) sector, which usually follows up a wintertime El
101 Niño–Southern Oscillation event and persists into the summer through the capacitor effect (Klein et al., 1999; Yang et al.,
102 2007; Xie et al., 2009). It is worth noting that the IOBM also features a basin-scale warming/cooling at interdecadal
103 timescales (Han et al., 2014), exerting active impacts on the mid-latitude Asian climate (e.g., Wu et al., 2016; Li and Ma,
104 2018; Zhang et al., 2018; S. Wang et al., 2022). As for the interdecadal variations of the summer EAMBZ precipitation,
105 we hope to answer the following two questions: 1) Did the JJA EAMBZ precipitation feature interdecadal variations? If
106 so, 2) is there any intimate connection between IOBM and the EAMBZ precipitation at interdecadal timescales? As such,
107 this study shall extend previous studies by exploring what extent and how the JJA IOBM modulate the concurrent EAMBZ
108 precipitation variability at interdecadal timescales, with the aim of providing a novel understanding for the rainfall
109 variability over the mid-latitude semi-arid zone in Asia. Note that we employ datasets with a centennial scale in this study
110 [e.g., the precipitation data produced by the Climatic Research Unit (CRU) and the atmospheric circulation data from the
111 Twentieth Century Reanalysis datasets]. In comparison with the short-term datasets since the latter half of the 20th century,
112 these long-term datasets can separate the interdecadal variability of EAMBZ precipitation from the externally forced
113 global climate change caused by anthropogenic (e.g., greenhouse gas) and natural forcings (e.g., volcanic eruption) more
114 effectively (Wu et al., 2016), which were widely used to investigate the physical causes of how internal fluctuations of
115 the climate system modulate the interdecadal variations of precipitation over Asia (e.g., Wu et al., 2016; Zhang et al.,
116 2018; Sun et al., 2019a; Jiang et al., 2021; J. Wang et al., 2022).

117

118 The remainder of this paper is arranged as follows. Section 2 describes the datasets and methods used in this study. Section
119 3 elucidates the characteristics of the interdecadal variations of summertime EAMBZ precipitation and the associated
120 background circulations, illustrates the mechanisms of how IOBM modulates the EAMBZ precipitation, establishes a
121 linear regression model using the IOBM to predict the interdecadal precipitation anomalies over EAMBZ, and verifies
122 the IOBM-related physical processes using numerical model simulations. A summary of the major findings and further
123 discussions are provided in Section 4.

124

125 2 Datasets and methods

126

127 2.1 Observational Data

128

129 Several monthly mean observational datasets are utilized in the present study, including (1) the global land high-resolution

130 gridded CRU time series precipitation dataset version 3.26 (CRU TS3.26; spatial resolution: $0.5^\circ \times 0.5^\circ$; Harris et al., 2014)
 131 for 1901–2017, (2) the Extended Reconstructed SST version 5 (ERSSTv5; spatial resolution: $2^\circ \times 2^\circ$; B. Huang et al., 2017)
 132 for 1854–present derived from the National Oceanic and Atmospheric Administration (NOAA), and (3) atmospheric
 133 variables derived from NOAA–Cooperative Institute for Research in Environmental Sciences (CIRES) Twentieth Century
 134 Reanalysis version 2c (20CRv2c; spatial resolution: $2^\circ \times 2^\circ$; Compo et al., 2011), except for the precipitation data, with
 135 192 points in longitude and 94 points in latitude, for 1851–2014. Note that all observational datasets cover the common
 136 time period of 1901–2014, which is the focused period in the present research.

137

138 2.2 Rossby wave source

139

140 Following Sardeshmukh and Hoskins (1988), the Rossby wave source (RWS) is calculated as:

$$141 \quad RWS = -\nabla \cdot [\mathbf{V}_\chi (\zeta + f)], \quad (1)$$

142 where \mathbf{V}_χ is the divergent wind, ζ is the relative vorticity, and f is the planetary vorticity.

143

144 2.3 Moisture flux and associated divergence

145

146 The vertically integrated horizontal water vapor transport ($\langle WVT \rangle$) and WVT-associated divergence ($\langle WVT_div \rangle$) are
 147 calculated using the following equations (Sun et al., 2019b; J. Wang et al., 2022):

$$148 \quad \langle WVT \rangle = -\frac{1}{g} \int_{P_s}^{300} q \vec{V} dp, \quad (2)$$

$$149 \quad \langle WVT_div \rangle = -\frac{1}{g} \int_{P_s}^{300} \nabla_p \cdot (q \vec{V}) dp, \quad (3)$$

150 where $\nabla_p \cdot ()$ denotes the horizontal divergence in the pressure coordinates; g is the gravitational acceleration; P_s is the

151 surface pressure; q is the specific humidity; and $\vec{V} = (u, v)$ is the horizontal wind vector (u and v represent the zonal and

152 meridional winds, respectively).

153

154 2.4 Statistical methods

155

156 This study focuses on interdecadal fluctuations in variables. The data are 11-year low-pass filtered by adopting a Lanczos
 157 filter (Duchon, 1979) to extract the corresponding interdecadal signal. Several statistical methods are used, including
 158 empirical orthogonal function (EOF) analysis, composite analysis, correlation analysis, and linear regression analysis. A
 159 two-tailed Student's t test is used to evaluate the statistical significance. Considering the 11-year low-pass filtered method
 160 can significantly reduce the degrees of freedom of the data, the following approximation is therefore deployed to calculate
 161 the effective degrees of freedom (N^{eff}):

$$162 \quad \frac{1}{N^{eff}} \approx \frac{1}{N} + \frac{2}{N} \sum_{j=1}^N \frac{N-j}{N} \rho_{XX}(j) \rho_{YY}(j), \quad (4)$$

163 where N is the sample size, and $\rho_{XX}(j)$ and $\rho_{YY}(j)$ are the autocorrelations of two sampled time series X and Y ,
 164 respectively, at time lag j (Li et al., 2013).

165

166 In this study, we focus on the boreal summer season (JJA). All variables in observations and model simulations are
167 linearly detrended before further calculations and analyses to exclude potential impacts of long-term trends.

168

169 2.5 Definitions

170

171 2.5.1 The research domain of EAMBZ

172

173 From the long-term (1901–2014) perspective of the climatological mean state of converged <WVT> and pronounced
174 precipitation over the mid-latitude Asia, the EAMBZ (box in Figs. 1a and 1b; 35°–55°N, 105°–130°E) is defined as the
175 collision and convergence zone between JJA dry westerly <WVT> and moist southwesterly <WVT> (Fig. 1a). As such,
176 there exist wetter conditions over the EASM-dominated part and drier conditions over the westerly-controlled part (Fig.
177 1b), suggesting the semi-arid transitional feature of EAMBZ (Xing and Wang, 2017). Our defined research domain of
178 EAMBZ largely matches the monsoon boundary zone defined by Chen et al. (2021), covering Inner Mongolia, Gansu,
179 Ningxia, Shaanxi, Shanxi, Hebei, Beijing, Tianjin, Shandong, Jilin, Liaoning, and Heilongjiang in China, as well as
180 eastern Mongolia and Korean peninsula. Note that our focused EAMBZ domain differs from the Northeast Asian domain
181 (29°–50°N, 108°–140°E) suggested by Si et al. (2021). Although they are extensively overlapped, the EAMBZ is located
182 more westward and northward, and defined from the climatic system perspective, not from a pure geographical
183 perspective. Since the areal mean precipitation over EAMBZ in boreal summer is the highest of the year accompanying
184 the largest standard deviation (i.e., largest rainfall variability) (Fig. S1), the summer season is focused in the present study.

185

186 2.5.2 Climate indices

187

188 The IOBM index (I_{IOBM}) is defined as areal mean SSTAs over the TIO domain of 20°S–20°N, 40°–100°E (Xie et al.,
189 2009). The IPO index is calculated using a method identical to that defined in Henley et al. (2015), that is, the difference
190 between SSTAs averaged over the central equatorial Pacific (10°S–10°N, 170°E–90°W) and the average of SSTAs in the
191 northwest (25°–45°N, 140°E–145°W) and the southwest Pacific (50°S–15°S, 150°E–160°W). In observations,
192 considering the coupled nature of IOBM and IPO at interdecadal timescales in boreal summer [cf. Fig. 2a in Wu et al.
193 (2016)], we hence remove the potential influence of the contemporaneous IPO on precipitation via eliminating the signal
194 forcing of IPO from the data of climate variables based on the partial regression technique, which is widely used in
195 previous studies (e.g., Dou and Wu, 2018; J. Wang et al., 2022).

196

197 2.6 Model simulations

198

199 To validate our proposed mechanisms of how the TIO SSTAs (i.e., IOBM-associated SSTAs) remotely modulate the
200 summer EAMBZ precipitation on interdecadal timescales, following the method of Zhang et al. (2019) and Yang et al.
201 (2020), we adopt monthly mean outputs from two experiments of the Community Earth System Model version 1 (CESM1),
202 which is a fully coupled Earth system model incorporating components of atmosphere, ocean, land, and sea ice (Hurrell
203 et al., 2013).

204

205 The first experiment is the CESM1 Large Ensemble Numerical Simulation (referred to as CESM1_LENS; Kay et al.,
206 2015). Among total 40 ensemble members in CESM1_LENS (Yang et al., 2020), we use the first 35 individual members
207 according to many previous studies (e.g., Touma et al., 2021; J. Wang et al., 2023), which were completed at the climate
208 modeling center of National Center for Atmospheric Research (NCAR). Note that all ensemble members in

209 CESM1_LENS were imposed with the same radiative forcing scenario (Taylor et al., 2012), with historical forcing for
210 1920–2005 and high-emission forcing scenario (i.e., Representative Concentration Pathway 8.5) for 2006–2080 (Moss et
211 al., 2010; Touma et al., 2021). The ensemble members were further generated with slightly differentiated perturbations
212 of atmospheric states (Kay et al., 2015; Touma et al., 2021). The second experiment is the CESM1 Indian Ocean
213 Pacemaker Ensemble Simulation (referred to as CESM1_IOPES), with 10 ensemble members (Zhang et al., 2019; Yang
214 et al., 2020). We adopt CESM1_IOPES to highlight the impact of SSTAs over the broader TIO domain (15°S–15°N,
215 African coast to 174°E). For the convenience of subsequent calculations and analyses, the African coast is designated as
216 40°E in this study, and a small change in the longitudes regarding the African coast may not affect the main results.

217
218 As indicated by Yang et al. (2020), the CESM1_LENS 35-member ensemble mean results can better provide an estimate
219 of the influence of the ~~external radiative forcing signals (e.g., greenhouse gas) due to external perturbations such as~~
220 ~~greenhouse gases~~ on the climate system. Furthermore, the 10-member ensemble mean results in CESM1_IOPES contain
221 the responses to both the time-evolving radiative forcing due to external perturbations and the restored observed time-
222 varying SSTAs over the above broader TIO domain (Yang et al., 2020). Note that though the ozone forcing data used in
223 CESM1_IOPES differ from those in CESM1_LENS, the differences in the corresponding simulated tropical and
224 extratropical climates were indistinguishable (e.g., Schneider et al., 2015; Schneider and Deser, 2018; Zhang et al., 2019;
225 Yang et al., 2020). Therefore, by subtracting the CESM1_LENS ensemble mean from the CESM1_IOPES ensemble mean
226 (i.e., removing the shared radiative forcing described above), we can obtain the response of the climate system to the
227 internal variability stemming from the time-varying SSTAs over the specific TIO, isolating the intrinsic climate variability
228 driven by TIO SSTAs through excluding the impacts of the time-evolving external radiative forcing. More details about
229 CESM1_LENS and CESM1_IOPES can be found in Kay et al. (2015) and Yang et al. (2020), respectively. The variables
230 employed here comprise precipitation and wind in atmosphere component of Community Atmospheric Model version 5,
231 with a spatial resolution of 1.25° in longitude and 0.9° in latitude; and SST in the ocean component of Parallel Ocean
232 Program version 2, with 320 grids in longitude and 384 grids in latitude. Before further analyses, model outputs are
233 interpolated at a resolution of 2°×2° using a bilinear interpolation method (Mastyło, 2013), identical to that of 20CRv2c.
234 In the current study, we focus on the historical simulation period of 1920–2005.

235
236 Here, it is important to stress the following two points. First, although the TIO domain in CESM1_IOPES is broader than
237 that for defining I_{IOBM} , there exist highly consistent temporal variations in SSTAs between them in observations (Fig. S2)
238 and simulations (Fig. S3) at interdecadal timescales, with temporal correlation coefficients (TCCs) of 0.93 and 0.87 ($P <$
239 0.01), respectively. Second, when selecting the SSTAs over the broader TIO domain (purple box in Fig. S4) as a metric,
240 it can be found that the observed (Fig. S4a) and modelled (Fig. S4b) large and intense loadings of the positive SSTAs are
241 still concentrated around the narrower TIO domain (black box in Fig. S4). As such, it is plausible to adopt the above-
242 mentioned Indian Ocean pacemaker experiment with broader TIO SSTAs to validate our proposed mechanisms tied to
243 the interdecadal IOBM variations.

244 245 3 Results

246 247 3.1 Observed interdecadal variations of the summer precipitation over EAMBZ and related 248 background circulations

249
250 Figure 1c plots the spatial distribution of the interdecadal standard deviation of precipitation. This distribution is quite
251 similar to that of the climatology (Fig. 1b), suggesting relatively strong (weak) interdecadal precipitation fluctuations

252 over the EASM-dominated (westerly-controlled) part of the EAMBZ. Moreover, we show the first EOF mode of JJA-
253 mean EAMBZ precipitation (Fig. 1d), which accounts for 28% of the total variance and distinguishes from the remaining
254 eigenvectors according to the criterion defined by North et al. (1982). The leading EOF mode bears close resemblance to
255 the standard deviation of the EAMBZ precipitation on interdecadal timescales (Figs. 1c and 1d), with larger loadings
256 occupying the Bohai Sea and Korean peninsula and their adjoining regions. The interdecadal TCC between the principal
257 component of the EOF1 and area-averaged precipitation over the research domain of EAMBZ (35° – 55° N, 105° – 130° E)
258 [EAMBZ precipitation index (I_{EAMBZP} for short); Fig. 1e] is 0.93 ($P < 0.001$). The aforementioned results indicate that
259 that our defined I_{EAMBZP} can serve as a good indicator of the predominant fluctuations in the precipitation anomalies over
260 EAMBZ at interdecadal timescales. As such, from the time series of 11-year low-passed filtered I_{EAMBZP} (Fig. 1e), we can
261 observe that the summer EAMBZ precipitation delineates notable interdecadal fluctuations. For example, EAMBZ
262 experienced dry summers during the periods preceding 1927, 1939–1945, 1968–1982, and 1998–2010, but underwent
263 wet summers during the periods of 1928–1938, 1946–1967, and 2011 onwards. Note that to some extent, the observed
264 major interdecadal fluctuation periods of summertime EAMBZ precipitation are dissimilar from those tied to summertime
265 Northeast Asian precipitation revealed by observations (1900–2012) from 11 local meteorological stations (Si et al., 2021),
266 e.g. the above-normal precipitation over EAMBZ (Fig. 1e) vs. the below-normal precipitation over Northeast Asia around
267 1990 (Si et al., 2021; their Fig. 2a).

268
269 Before examining the modulation of IOBM on the interdecadal EAMBZ precipitation fluctuations, it is essential to
270 scrutinize the JJA-mean I_{EAMBZP} -associated circulation anomalies. The highest mid-latitude positive correlation region
271 can be discerned north of the TP (38° – 46° N, 80° – 112.5° E; blue box in Fig. 2a), suggesting that the interdecadal
272 enhancement of the summer EAMBZ precipitation is intimately correlated with the acceleration of the upstream mid-
273 latitude westerlies at 400 hPa. In light of the method of Chen et al. (2021) and J. Wang et al. (2022), we correlate the
274 I_{EAMBZP} with the zonal winds averaged over the longitudinal range of EAMBZ at multiple levels (Fig. 2b) to further check
275 whether the most significant correlation occurs at 400 hPa. Evidently, on interdecadal timescales, the largest positive
276 correlation between precipitation and mid-latitude westerlies within 38° – 46° N does occur at the mid-tropospheric level
277 of 400 hPa, with a TCC of 0.46 ($P < 0.01$) between the I_{EAMBZP} and areal mean 400-hPa zonal winds over the upstream
278 westerly-dominated domain (Fig. 2c). Note that this correlation pattern exhibits a barotropic structure (Fig. 2b).
279 Additionally, we correlate the I_{EAMBZP} with the 850-hPa meridional winds. The I_{EAMBZP} is positively correlated with the
280 key monsoonal southerly domain east of the TP (25° – 33° N, 102.5° – 112.5° E; green box in Fig. 2d), which is located in
281 the western portion of the EASM domain (Ying et al., 2023). The interdecadal correlation pattern between meridional
282 winds and the summer EAMBZ precipitation at multiple levels exhibits a baroclinic structure, with the significant positive
283 correlations confined below 500 hPa (Fig. 2e). Note that the strongest positive correlation is detected at 850 hPa within
284 102.5° – 112.5° E, with a TCC of 0.63 (Fig. 2f; $P < 0.001$) between I_{EAMBZP} and areal mean 850-hPa meridional winds over
285 the key EASM-controlled domain (Fig. 2d).

286
287 Figure 3 gives the JJA-mean I_{EAMBZP} -regressed circulation anomalies at interdecadal timescales. The interdecadal
288 enhancement of the EAMBZ precipitation is significantly linked to a localized quasi-barotropic cyclonic (low-pressure)
289 anomaly. At 400 hPa, significant westerly anomalies prevail in its southern flank, inducing the acceleration of westerlies
290 upstream of EAMBZ (Fig. 3a). At 850 hPa, the enhanced EAMBZ precipitation is connected to a north-south meridional
291 seesaw pattern, with a significant anticyclonic (high-pressure) anomaly over the subtropical western Pacific (SWP) and a
292 significant cyclonic anomaly over EAMBZ (Fig. 3b), exhibiting a somewhat barotropic structure (Figs. 3a and 3b).
293 Significant southerly anomalies prevail in the western flank of this SWP clockwise gyre anomaly (SWPCGA). Moreover,
294 from the perspective of $\langle WVT \rangle$ (Fig. 3c), the magnitudes of southerly $\langle WVT \rangle$ anomalies over the key EASM-controlled

295 domain tied to the SWPCGA are much greater than the westerly $\langle WVT \rangle$ anomalies over the westerly-dominated domain.
296 Note that the southerly $\langle WVT \rangle$ anomalies are significantly divergent, pushing copious amounts of warm and moist vapor
297 over the SWP into EAMBZ. Then, with the aid of the local anticlockwise $\langle WVT \rangle$ gyre pattern (Fig. 3c), the EASM
298 southerlies from the low latitudes, which bring warm temperature advection anomalies, may easily collide with the mid-
299 level cold temperature advection anomalies brought by mid-latitude enhanced westerlies (Figs. 4a and 4b), manifesting
300 the extratropical–tropical interplay around EAMBZ on interdecadal timescales. Such interplay is basically aligned with
301 that on interannual timescales (cf. Chen et al., 2021). Under such environments, atmospheric instability over EAMBZ can
302 be triggered to generate in situ significant ascending motion anomalies responsible for increased precipitation (Fig. 5a).
303 Note that considering the greater magnitudes of anomalies of $\langle WVT \rangle$ and warm temperature advection connected to the
304 southerlies over the key EASM-controlled domain, we presume that the monsoonal southerlies play a predominant
305 dynamical role in the interdecadal enhancement of precipitation over EAMBZ. To verify this presumption, we further
306 propose an East Asian monsoon index (I_{MI} for short), defined as the areal mean meridional winds at 850 hPa over the key
307 monsoonal southerly domain, and a westerly index (I_{WI} for short), defined as the areal mean 400-hPa zonal winds over
308 the upstream westerly-dominated region. The I_{MI} -regressed results can well and realistically reproduce the magnitudes
309 and distributions of the anomalous upward motions tied to I_{EAMBZP} (Fig. 5b vs. 5a). However, the magnitudes of I_{WI} -
310 regressed results are highly weakened, along with the major loadings shifting more southward (Fig. 5c). Above results
311 could allow us to conclude that the anomalous southerlies over the key monsoonal southerly domain could be the
312 predominant driving factor for the interdecadal enhancement of summer EAMBZ precipitation, whereas the upstream
313 accelerated westerlies play a secondary dynamical amplification role.

314

315 3.2 Interdecadal relationship between IOBM and the summer EAMBZ precipitation

316

317 Many previous studies have substantiated that the IOBM can remotely modulate summer rainfall fluctuations over the
318 mid-latitude Asia at interdecadal timescales (e.g., Zhang et al., 2018; S. Wang et al., 2022; Wu et al., 2022). Note that the
319 existing studies primarily highlighted the impacts of IOBM on the summer rainfall variations over northwest portion of
320 the mid-latitude Asia a (e.g., S. Wang et al., 2022; Wu et al., 2022). As for the work of Zhang et al. (2018), although this
321 study focused the northeast portion of the mid-latitude Asia including the EAMBZ, it highlighted the combined roles of
322 IOBM, AMO and PDO. In the present study, however, we identify that it is the IOBM that may exert profoundly
323 simultaneous impacts on the interdecadal variations of the EAMBZ precipitation in boreal summer, which will be revealed
324 subsequently.

325

326 Figure 6a exhibits the correlation pattern between the JJA-mean I_{EAMBZP} and the contemporaneous global gridded SST at
327 interdecadal timescales. The most pronounced and significant correlations are found in the TIO sector, which largely
328 matches the domain for delineating the IOBM mode (black frame in Fig. 6a). There exists a salient out-of-phase
329 relationship between the interdecadal EAMBZ precipitation changes and the IOBM mode, with a TCC of -0.57 between
330 I_{EAMBZP} and I_{IOBM} (Fig. 6b; $P < 0.01$). This result suggests that IOBM warming (cooling) is significantly connected with
331 dry (wet) EAMBZ summers, which serves as a critical oceanic modulator. On interdecadal timescales, the IOBM can
332 remotely spark conducive dynamical circumstances for increased precipitation over EAMBZ, i.e., the collision between
333 cold and warm airflows around EAMBZ (Figs. 4c and 4d) and the locally significant convergent ascending motion
334 anomalies resembled those tied to the positive I_{EAMBZP} (Fig. 5d vs. 5a). However, the extratropical cold (tropical warm)
335 temperature advection anomalies west (south) of the EAMBZ, which are tied to the strengthened westerlies (southerlies),
336 are quite insignificant (significant) (Figs. 4c and 4d). This indicates that the IOBM may exerts a more profound influence
337 on the southerly wind anomalies over the EASM-controlled domain, which is more important for enhanced EAMBZ

338 precipitation; whereas the IOBM may insignificantly modulate the westerly anomalies over the westerly-dominated
339 region. The possible underlying mechanisms of how IOBM links the summertime circulation anomalies responsible for
340 the interdecadal fluctuations in the EAMBZ precipitation will be illuminated in the next subsection.

341

342 3.3 Possible mechanisms

343

344 Figure 7 shows partial regression of the JJA-mean anomalies of SST and large-scale precipitation over TIO and its
345 neighboring areas onto the I_{IOBM} at interdecadal timescales with the IPO signal forcing removed. Corresponding to higher
346 I_{IOBM} years, warm SSTAs cover almost all areas of TIO, with large loadings appearing in the central-southern TIO and
347 relatively small loadings appearing in the northern TIO (Fig. 7a), which are aligned with the previous studies (Wu et al.,
348 2016; Y. Huang et al., 2019). Moreover, there are striking suppressed precipitation around the northeast corner of the TIO
349 domain (Fig. 7b), suggesting profoundly localized atmospheric responses (viz. the release of regional anomalous
350 atmospheric cooling) to the warm TIO SSTAs. Note that corresponding to cold TIO SST years, there exist positive
351 precipitation anomalies around the northeast corner of TIO, suggesting the release of anomalous atmospheric heating
352 (figure not shown). Since the significant out-of-phase relationship between summertime IOBM and EAMBZ precipitation
353 at interdecadal timescales, we adopt negative I_{IOBM} -regressed patterns to express the influence of cold SSTAs over the
354 TIO region. Figure 8 displays the anomalous patterns of the RWS, velocity potential, and divergent horizontal winds
355 regressed onto the negative I_{IOBM} . The velocity potential anomalies with larger negative (positive) loadings in the upper
356 (lower) troposphere are concentrated surrounding the northeast corner of TIO. Under these circumstances, local upper
357 (lower) tropospheric divergence (convergence) and negative (positive) RWS anomalies can be observed (Fig. 8),
358 suggesting enhanced ascending motions and convection activities in situ and thereby exciting the localized increased
359 precipitation/atmospheric heating. The above results indicate that IOBM cooling may transmit its interdecadal influence
360 via the intermediate atmospheric bridge of enhanced convective activities around the northeast corner of TIO, exerting a
361 remote modulation on an interdecadal enhancement of the EAMBZ rainfall.

362

363 Next, we further discuss the physical pathway linking IOBM cooling with the far-reaching downstream circulation
364 anomalies responsible for the interdecadal enhancement of EAMBZ precipitation, as shown in Fig. 9. Because the
365 cyclonic anomaly at 400 hPa shifts more eastward compared to the I_{EAMBZP} -regressed counterpart (Fig. 9a vs. 3a), only
366 fractional westerly anomalies occupy the eastern part of the westerly-dominated region. The TCC between I_{IOBM} and I_{WI}
367 is nearly equal to zero ($r = -0.06$), thus linking the insignificant cold temperature advection displayed in Fig. 4c.
368 Nevertheless, in the lower troposphere, a “north-low–south-high” meridional seesaw pattern over the Northeast China–
369 SWP sector is found to be linked with IOBM cooling (Fig. 9b). Note that this negative I_{IOBM} -regressed seesaw pattern
370 exhibits a quasi-barotropic structure, with an anticlockwise <WVT> gyre in the north and a SWPCGA in the south (Fig.
371 9c), which is highly similar to that shown in Fig. 3. Significant anomalies of 850-hPa meridional winds and southerly
372 <WVT> prevail over the key monsoonal southerly domain, lying on the western flank of SWPCGA (Figs. 9b and c). The
373 TCC between I_{IOBM} and I_{MI} is -0.33 , significant at 0.05 on interdecadal timescales, thereby linking the significant warm
374 temperature advection anomalies indicated in Fig. 4d.

375

376 One may ask how IOBM cooling induces the above-mentioned meridional seesaw pattern. Previously, we have revealed
377 that negative SSTAs over TIO may exert remote interdecadal impacts through an atmospheric bridge, i.e., vigorous
378 convective activities around the northeast corner of TIO (Figs. 7 and 8). In effect, there exists a low-level cyclonic
379 anomaly in situ (Fig. 9b). Such cyclonic anomaly can be interpreted as a typical Gill–Matsuno-type response (Matsuno,
380 1966; Gill, 1980) to the regional anti-symmetric atmospheric heating caused by IOBM cooling with the coldest center

381 located south of the equator, which is more clear within the lower levels (Fig. 9b). As a result, consistent easterly
 382 anomalies appear from SWP to its northern flank around 15°N, denoting the active role of depressed air pressure. The
 383 consistent easterly anomalies over SWP could lead to local anticyclonic wind shear anomalies (Wang et al., 2019). In
 384 such a scenario, a quasi-barotropic SWPCGA can be induced (Fig. 9c). Further, local downward motions tied to SWPCGA
 385 could induce significant upward motions to its north via a meridional overturning circulation (J. Wang et al., 2021), thus
 386 exciting a quasi-barotropic cyclonic anomaly and an anticlockwise <WVT> gyre pattern centered over Northeast China
 387 (Figs. 9a–c). Therefore, positive summertime rainfall anomalies over EAMBZ at interdecadal timescales can be induced
 388 (Fig. 9d). Notably, circulation and precipitation anomalies during the warm phase years of the IOBM (Fig. S5) highly
 389 mirror those tied to the IOBM cooling with opposite signs.

390

391 3.4 Results from CESM1 simulations

392

393 In this subsection, we use the pacemaker experimental data based on the ensemble mean of CESM1_IOPES and
 394 CESM1_LENS to validate our proposed mechanisms regarding the modulation of IOBM cooling on the interdecadal
 395 enhancement of summer EAMBZ precipitation. Considering the predominant role of southerly anomalies over the key
 396 monsoonal southerly domain, we therefore emphasize the low-level (850 hPa) atmospheric anomalies at interdecadal
 397 timescales tied to the IOBM-like SST cooling, as depicted in Fig. 10. We can observe a clearly anomalous cyclonic
 398 circulation around the northeast corner of TIO, accompanied by local positive precipitation anomalies and easterly
 399 anomalies that stretch from SWP to its northern flank, which are generally resembled those in the observation (Fig. 9). In
 400 this circumstance, a similar “north-low–south-high” meridional seesaw pattern over the Northeast China–SWP sector can
 401 be simulated to spark and sustain the enhanced EAMBZ precipitation in boreal summer (Fig. 10). In summary, by and
 402 large, the ensemble mean composite results can well reproduce the observed anomalous circulation and precipitation
 403 driven by IOBM-related SSTAs, confirming the crucial role of IOBM cooling in driving enhanced summer precipitation
 404 over EAMBZ at interdecadal timescales.

405

406 3.5 Estimation of the interdecadal variations of summer EAMBZ precipitation

407

408 In the last three subsections, we suggest that the IOBM cooling can serve as a significant oceanic modulator for increased
 409 summer EAMBZ precipitation at interdecadal timescales based on observation evidences and pacemaker experiments,
 410 and present the corresponding physical mechanisms. To estimate their steady antiphase relationship, in the following, the
 411 negative I_{IOBM} is selected to construct a physical-based empirical model by using the simple linear regression analysis and
 412 the cross-validation method (You and Jia, 2018; Chang et al., 2021; Jeong et al., 2021), representing the impact of IOBM
 413 cooling. The physical-based model is given as follows:

414

$$415 I_{EAMBZP} = \beta_0 + \beta_1 I_{IOBM} + \varepsilon, \quad (5)$$

416

417 where β_0 and β_1 are regression coefficients, and ε denotes the residuals. The time series of I_{EAMBZP} and I_{IOBM} are detrended
 418 and 11-year low-pass filtered beforehand.

419

420 Following the method of Jeong et al. (2021), a “leaving one out” cross-validation strategy is employed to determine the
 421 robustness of the hindcast estimates. The normalized time series of summer I_{EAMBZP} and associated leave-one-out cross-
 422 validated hindcast estimates are shown in Fig. 11. The TCC between the physical-based predicted hindcast estimates (blue
 423 line) and the observed I_{EAMBZP} (red line) for 1901–2014 can reach 0.56 ($P < 0.05$), suggesting that the physical-based

424 model can well capture the interdecadal I_{EAMBZP} variations and reflect their steady relationship.

425

426 Although our proposed physical-based empirical model could confirm the concurrently intimately interdecadal
427 relationship between IOBM and EAMBZ precipitation, we should acknowledge the shortcomings of the model.
428 First, the amplitudes of the hindcast estimates are fairly lower, which cannot well capture the extreme precipitation
429 years (e.g., years around 1960; Fig. 11). Second, the simultaneous [signal-forcing](#) of IOBM cannot be served as a
430 predictor for summertime EAMBZ precipitation variations. As such, this model inherently lacks the ability to
431 predict the interdecadal EAMBZ precipitation anomalies in advance.

432

433 4 Conclusions and discussion

434

435 In this study, by analysis of the long-term observational and reanalysis datasets during 1901–2014, the temporal
436 characteristics of interdecadal variations in the summer EAMBZ precipitation and associated circulation background are
437 revealed. The potential modulation of IOBM on the variations is further discussed. As a summary of our major findings,
438 Fig. 12 schematically synthesizes how IOBM-associated SST mode remotely drives the interdecadal precipitation
439 fluctuations via a tropical route.

440

441 The summer EAMBZ precipitation exhibited a salient interdecadal fluctuations, e.g., with dry summers during the periods
442 preceding 1927, 1939–1945, 1968–1982, and 1998–2010, as well as wet summers during the periods of 1928–1938,
443 1946–1967, and 2011 onwards. It is indicated that the cold airflows brought by the mid-latitude accelerated upstream
444 westerlies over the westerly-dominated domain collide and converge with the warm and humid airflows brought by the
445 enhanced southerlies over the key EASM-controlled domain, suggesting the local extratropical–tropical interplay. Further
446 diagnostic results suggest that the monsoonal southerly anomalies could be viewed as the predominant driving factor for
447 the interdecadal enhancement of EAMBZ precipitation, whereas the upstream westerlies play a secondary dynamical
448 amplification role. Such circulation anomalies are closely linked to a “north-low–south-high” meridional seesaw pattern
449 over the Northeast China–SWP sector, which provides favorable environments for the transportation of water vapor from
450 the SWP and the convergence over EAMBZ to spark enhanced summer EAMBZ precipitation at interdecadal timescales.

451

452 We further identify that the IOBM-related SST anomaly pattern is a salient oceanic forcing for the interdecadal variations
453 of the summer EAMBZ precipitation via the Gill–Matsuno mechanism, [playing an independent and critical modulation](#)
454 [role](#). When the cold phase of the IOBM occurs, an anomalous cyclonic circulation is excited around the northeast corner
455 of TIO in terms of the regional anti-symmetric atmospheric heating. As a response, consistent easterly anomalies appear
456 from SWP to its northern flank, leading to local anticyclonic wind shear anomalies and thus inducing a SWPCGA pattern
457 and a resultant anticlockwise gyre pattern centered over Northeast China. On interdecadal timescales, such meridional
458 seesaw pattern tied to the IOBM cooling is responsible for enhanced summer precipitation over EAMBZ through linking
459 the predominant driving factor of strengthened monsoonal southerly anomalies west of the SWPCGA pattern. As such,
460 the water vapor transportation from the SWP and the convergence over EAMBZ can be triggered to induce and sustain
461 the enhancement local precipitation. Correspondingly, a physical-based model based the negative I_{IOBM} is constructed,
462 which can well capture the interdecadal fluctuations in the EAMBZ precipitation and reflect their steady relationship.
463 Furthermore, the results based on the large ensemble experiment and the Indian Ocean pacemaker experiment also
464 confirm the crucial physical pathway linking the SST variations over TIO with the summer precipitation over EAMBZ
465 via the influence of SST variations on the aforementioned meridional seesaw pattern at interdecadal timescales.

466

467 The following two points deserve further discussion. First, although results from CESM1_LENS and CESM1_IOPES
468 can reasonably confirm our proposed physical pathway of how IOBM cooling exerts a distant modulation on the
469 interdecadal enhancement of summer precipitation over EAMBZ, we can still notice the weakness of the model
470 simulations. That is, positive precipitation anomalies around the northeast corner of TIO and the easterly anomalies
471 exhibit weaker magnitudes compared to the observations (Fig. 10 vs. 7b and 9b). Besides, systematic biases exist
472 regarding the simulated positions of the upper (lower) tropospheric divergence (convergence) and negative (positive)
473 RWS anomalies (Fig. S6), manifesting themselves in the eastward displacement tendency in contrast to those around the
474 northeast corner of the TIO (Fig. 8).

475

476 Second, this study merely identifies the physical linkage between the interdecadal summer EAMBZ precipitation
477 and the contemporaneous SST mode over the TIO basin from the tropical route. Nonetheless, the contemporaneous
478 IOBM is not a predictor. According to many previous studies (e.g., Wang et al., 2015; Li et al., 2023), the physical-
479 based empirical model based on multiple predictors may better improve the forecast skill. Thus, it is urgent to find
480 out more salient precursor signalsforcings of the lower boundary anomalies [e.g., sea ice (Han et al., 2021)] and
481 figure out associated mechanisms for interdecadal EAMBZ precipitation changes to construct an effective prediction
482 model.

483

484

485 Code and data availability. The CRU time series precipitation data version 3.26 (CRU TS3.26) from CRU at the University
486 of East Anglia are available online (<https://catalogue.ceda.ac.uk/uuid/3f8944800cc48e1cbc29a5ee12d8542d>; CRU, 2022).
487 The ERSSTv5 data from the US NOAA are available from the following website:
488 <https://www1.ncdc.noaa.gov/pub/data/cmb/ersst/v5/netcdf/> (NOAA 2020). The 20CRv2c datasets from NOAA-CIRES
489 are available from the following website: https://psl.noaa.gov/data/gridded/data.20thC_ReanV2c.html (NOAA-CIRES,
490 2022). The model simulation datasets regarding CESM1_LENS are available online
491 (<https://www.cesm.ucar.edu/community-projects/lens/data-sets>; NCAR 2023). The model simulation datasets regarding
492 CESM1_IOPES are available online (<https://www.earthsystemgrid.org/dataset/ucar.cgd.cesm4.IOD-PACEMAKER.html>;
493 NCAR 2023).

494 Codes are available from the corresponding author on reasonable request.

495

496 Author contributions. YL designed the research; JW wrote the first draft of the paper; FC and CS downloaded and
497 analyzed the data, and plotted the figures used in this study. All authors, including QL, YD, and XX, contributed to the
498 discussion of the results and reviewed the manuscript.

499

500 Competing interests. The contact author has declared that none of the authors has any competing interests.

501

502 Disclaimer. Publisher's note: Copernicus Publications remains neutral with regard to jurisdictional claims made in the
503 text, published maps, institutional affiliations, or any other geographical representation in this paper. While Copernicus
504 Publications makes every effort to include appropriate place names, the final responsibility lies with the authors.

505

506 Acknowledgements. Yanju Liu acknowledges the support by the Key Innovation Team of China Meteorological
507 Administration "Climate Change Detection and Response" (CMA2022ZD03).

508

509 Financial support. This study was supported by the Second Tibetan Plateau Scientific Expedition and Research (STEP)
510 program (2019QZKK010204-02 and 2019QZKK0102), Guangdong Major Project of Basic and Applied Basic Research

511 (2020B0301030004), and Innovation and Development Special Project of China Meteorological Administration
512 (CXFZ2022J039).

513

514

515 References

516

517 Chang, L., Wu, Z. and Xu, J., 2021. Contribution of Northeastern Asian stratospheric warming to subseasonal prediction
518 of the early winter haze pollution in Sichuan Basin, China. *Science of the Total Environment*, 751: 141823.

519 Chen, F.-H., Chen, J.-H., Holmes, J., Boomer, I., Austin, P., Gates, J.B., Wang, N.-L., Brooks, S.J. and Zhang, J.-W., 2010.
520 Moisture changes over the last millennium in arid central Asia: a review, synthesis and comparison with monsoon
521 region. *Quaternary Science Reviews*, 29(7): 1055-1068.

522 Chen, J., Huang, W., Feng, S., Zhang, Q., Kuang, X., Chen, J. and Chen, F., 2021. The modulation of westerlies-monsoon
523 interaction on climate over the monsoon boundary zone in East Asia. *International Journal of Climatology*,
524 41(S1): E3049-E3064.

525 Chen, J., Huang, W., Jin, L., Chen, J., Chen, S. and Chen, F., 2018. A climatological northern boundary index for the East
526 Asian summer monsoon and its interannual variability. *Science China Earth Sciences*, 61(1): 13-22.

527 Compo, G.P., Whitaker, J.S., Sardeshmukh, P.D., Matsui, N., Allan, R.J., Yin, X., Gleason, B.E., Vose, R.S., Rutledge, G.,
528 Bessemoulin, P., Brönnimann, S., Brunet, M., Crouthamel, R.I., Grant, A.N., Groisman, P.Y., Jones, P.D., Kruk,
529 M.C., Kruger, A.C., Marshall, G.J., Maugeri, M., Mok, H.Y., Nordli, Ø., Ross, T.F., Trigo, R.M., Wang, X.L.,
530 Woodruff, S.D. and Worley, S.J., 2011. The Twentieth Century Reanalysis Project. *Quarterly Journal of the Royal
531 Meteorological Society*, 137(654): 1-28.

532 CRU: CRU TS3.26, monthly, CRU [data set] <https://catalogue.ceda.ac.uk/uuid/3f8944800cc48e1cbc29a5ee12d8542d>,
533 last access: 5 July 2022.

534 Ding, Y. and Chan, J.C.L., 2005. The East Asian summer monsoon: an overview. *Meteorology and Atmospheric Physics*,
535 89(1): 117-142.

536 Dou, J. and Wu, Z., 2018. Southern Hemisphere origins for interannual variations of snow cover over the western Tibetan
537 Plateau in boreal summer. *Journal of Climate*, 31(19): 7701-7718.

538 Duchon, C.E., 1979. Lanczos filtering in one and two dimensions. *Journal of Applied Meteorology and Climatology*,
539 18(8): 1016-1022.

540 Gill, A.E., 1980. Some simple solutions for heat-induced tropical circulation. *Quarterly Journal of the Royal
541 Meteorological Society*, 106(449): 447-462.

542 Han, T., Zhang, M., Zhu, J., Zhou, B. and Li, S., 2021. Impact of early spring sea ice in Barents Sea on midsummer
543 rainfall distribution at Northeast China. *Climate Dynamics*, 57(3): 1023-1037.

544 Han, W., Vialard, J., McPhaden, M.J., Lee, T., Masumoto, Y., Feng, M. and de Ruijter, W.P.M., 2014. Indian Ocean
545 decadal variability: A review. *Bulletin of the American Meteorological Society*, 95(11): 1679-1703.

546 Harris, I., Jones, P.D., Osborn, T.J. and Lister, D.H., 2014. Updated high-resolution grids of monthly climatic
547 observations—the CRU TS3.10 Dataset. *International Journal of Climatology*, 34(3): 623-642.

548 Henley, B.J., Gergis, J., Karoly, D.J., Power, S., Kennedy, J. and Folland, C.K., 2015. A Tripole Index for the Interdecadal
549 Pacific Oscillation. *Climate Dynamics*, 45(11): 3077-3090.

550 Huang, B., Thorne, P.W., Banzon, V.F., Boyer, T., Chepurin, G., Lawrimore, J.H., Menne, M.J., Smith, T.M., Vose, R.S.
551 and Zhang, H.-M., 2017. Extended Reconstructed Sea Surface Temperature, version 5 (ERSSTv5): Upgrades,
552 validations, and intercomparisons. *Journal of Climate*, 30(20): 8179-8205.

553 Huang, J., Li, Y., Fu, C., Chen, F., Fu, Q., Dai, A., Shinoda, M., Ma, Z., Guo, W., Li, Z., Zhang, L., Liu, Y., Yu, H., He,
554 Y., Xie, Y., Guan, X., Ji, M., Lin, L., Wang, S., Yan, H. and Wang, G., 2017. Dryland climate change: Recent
555 progress and challenges. *Reviews of Geophysics*, 55(3): 719-778.

556 Huang, J., Ma, J., Guan, X., Li, Y. and He, Y., 2019. Progress in semi-arid climate change studies in China. *Advances in
557 Atmospheric Sciences*, 36(9): 922-937.

558 Huang, J., Zhang, G., Zhang, Y., Guan, X., Wei, Y. and Guo, R., 2020. Global desertification vulnerability to climate
559 change and human activities. *Land Degradation & Development*, 31(11): 1380-1391.

560 Huang, W., Chen, J., Zhang, X., Feng, S. and Chen, F., 2015. Definition of the core zone of the “westerlies-dominated
561 climatic regime”, and its controlling factors during the instrumental period. *Science China Earth Sciences*, 58(5):
562 676-684.

563 Huang, Y., Wu, B., Li, T., Zhou, T. and Liu, B., 2019. Interdecadal Indian Ocean basin mode driven by interdecadal
564 Pacific oscillation: A season-dependent growth mechanism. *Journal of Climate*, 32(7): 2057-2073.

565 Hurrell, J.W., Holland, M.M., Gent, P.R., Ghan, S., Kay, J.E., Kushner, P.J., Lamarque, J.F., Large, W.G., Lawrence, D.,
566 Lindsay, K., Lipscomb, W.H., Long, M.C., Mahowald, N., Marsh, D.R., Neale, R.B., Rasch, P., Vavrus, S.,
567 Vertenstein, M., Bader, D., Collins, W.D., Hack, J.J., Kiehl, J. and Marshall, S., 2013. The Community Earth
568 System Model: A framework for collaborative research. *Bulletin of the American Meteorological Society*, 94(9):
569 1339-1360.

570 Jeong, J.I., Park, R.J., Yeh, S.-W. and Roh, J.-W., 2021. Statistical predictability of wintertime PM_{2.5} concentrations over
571 East Asia using simple linear regression. *Science of the Total Environment*, 776: 146059.

572 Jiang, J., Zhou, T., Chen, X. and Wu, B., 2021. Central Asian precipitation shaped by the tropical Pacific decadal
573 variability and the Atlantic multidecadal variability. *Journal of Climate*, 34(18): 7541-7553.

574 Kay, J.E., Deser, C., Phillips, A., Mai, A., Hannay, C., Strand, G., Arblaster, J.M., Bates, S.C., Danabasoglu, G., Edwards,
575 J., Holland, M., Kushner, P., Lamarque, J.F., Lawrence, D., Lindsay, K., Middleton, A., Munoz, E., Neale, R.,
576 Oleson, K., Polvani, L. and Vertenstein, M., 2015. The community earth system model (CESM) large ensemble
577 project: a community resource for studying climate change in the presence of internal climate variability. *Bulletin
578 of the American Meteorological Society*, 96(8): 1333-1349.

579 Klein, S.A., Soden, B.J. and Lau, N.-C., 1999. Remote sea surface temperature variations during ENSO: evidence for a
580 tropical atmospheric bridge. *Journal of Climate*, 12(4): 917-932.

581 Li, J., Sun, C. and Jin, F.-F., 2013. NAO implicated as a predictor of Northern Hemisphere mean temperature multidecadal
582 variability. *Geophysical Research Letters*, 40(20): 5497-5502.

583 Li, J. and Zeng, Q., 2002. A unified monsoon index. *Geophysical Research Letters*, 29(8): 115-1-115-4.

584 Li, J., Zheng, C., Yang, Y., Lu, R. and Zhu, Z., 2023. Predictability of spatial distribution of pre-summer extreme
585 precipitation days over southern China revealed by the physical-based empirical model. *Climate Dynamics*,
586 61(5): 2299-2316.

587 Li, M. and Ma, Z., 2018. Decadal changes in summer precipitation over arid northwest China and associated atmospheric
588 circulations. *International Journal of Climatology*, 38(12): 4496-4508.

589 Lu, W. and Jia, G., 2013. Fluctuation of farming-pastoral ecotone in association with changing East Asia monsoon climate.
590 *Climatic Change*, 119(3): 747-760.

591 Mastyo, M., 2013. Bilinear interpolation theorems and applications. *Journal of Functional Analysis*, 265(2): 185-207.

592 Matsuno, T., 1966. Quasi-geostrophic motions in the equatorial area. *Journal of the Meteorological Society of Japan*,
593 44(1): 25-43.

594 Moss, R.H., Edmonds, J.A., Hibbard, K.A., Manning, M.R., Rose, S.K., van Vuuren, D.P., Carter, T.R., Emori, S.,
595 Kainuma, M., Kram, T., Meehl, G.A., Mitchell, J.F.B., Nakicenovic, N., Riahi, K., Smith, S.J., Stouffer, R.J.,
596 Thomson, A.M., Weyant, J.P. and Wilbanks, T.J., 2010. The next generation of scenarios for climate change
597 research and assessment. *Nature*, 463(7282): 747-756.

598 NCAR: CESM1_LENS, monthly, NCAR [data set] <https://www.cesm.ucar.edu/community-projects/lens/data-sets>, last
599 access: 28 April 2023.

600 NCAR: CESM1_IOPES, monthly, NCAR [data set] [https://www.earthsystemgrid.org/dataset/ucar.cgd.cesm4.IOD-
601 PACEMAKER.html](https://www.earthsystemgrid.org/dataset/ucar.cgd.cesm4.IOD-PACEMAKER.html), last access: 4 May 2023.

602 NOAA: ERSSTv5, monthly, NOAA [data set] <https://www1.ncdc.noaa.gov/pub/data/cmb/ersst/v5/netcdf/>, last access: 15
603 October 2020.

604 NOAA-CIRES: 20CRv2c, monthly, NOAA-CIRES [data set]
605 https://psl.noaa.gov/data/gridded/data.20thC_ReanV2c.html, last access: 26 June 2022.

606 North, G.R., Bell, T.L., Cahalan, R.F. and Moeng, F.J., 1982. Sampling errors in the estimation of empirical orthogonal
607 functions. *Monthly Weather Review*, 110(7): 699-706.

608 Ou, T.H. and Qian, W.H., 2006. Vegetation variations along the monsoon boundary zone in East Asia. *Chinese Journal of
609 Geophysics (in Chinese)*, 49(3): 698-705.

610 Piao, J., Chen, W. and Chen, S., 2021. Water vapour transport changes associated with the interdecadal decrease in the
611 summer rainfall over Northeast Asia around the late-1990s. *International Journal of Climatology*, 41(S1): E1469-
612 E1482.

613 Qian, W., Ding, T., Hu, H., Lin, X. and Qin, A., 2009. An overview of dry-wet climate variability among monsoon-
614 westerly regions and the monsoon northernmost marginal active zone in China. *Advances in Atmospheric
615 Sciences*, 26(4): 630-641.

616 Sardeshmukh, P.D. and Hoskins, B.J., 1988. The generation of global rotational flow by steady idealized tropical
617 divergence. *Journal of Atmospheric Sciences*, 45(7): 1228-1251.

618 Schiemann, R., Lüthi, D. and Schär, C., 2009. Seasonality and interannual variability of the westerly jet in the Tibetan
619 Plateau region. *Journal of Climate*, 22(11): 2940-2957.

620 [Schneider, D.P. and Deser, C., 2018. Tropically driven and externally forced patterns of Antarctic sea ice change: reconciling observed and modeled trends. *Climate Dynamics*, 50\(11\): 4599-4618.](#)

621

622 [Schneider, D.P., Deser, C. and Fan, T., 2015. Comparing the impacts of tropical SST variability and polar stratospheric ozone loss on the southern ocean westerly winds. *Journal of Climate*, 28\(23\): 9350-9372.](#)

623

624 Si, D. and Ding, Y., 2016. Oceanic forcings of the interdecadal variability in East Asian summer rainfall. *Journal of*

625 *Climate*, 29(21): 7633-7649.

626 Si, D., Jiang, D., Hu, A. and Lang, X., 2021. Variations in northeast Asian summer precipitation driven by the Atlantic

627 multidecadal oscillation. *International Journal of Climatology*, 41(3): 1682-1695.

628 Song, C., Wang, J., Liu, Y., Zhang, L., Ding, Y., Li, Q., Shen, X., Song, Y. and Yan, Y., 2022. Toward role of westerly-

629 monsoon interplay in linking interannual variations of late spring precipitation over the southeastern Tibetan

630 Plateau. *Atmospheric Science Letters*, 23(3): e1074.

631 Sun, B., Li, H. and Zhou, B., 2019a. Interdecadal variation of Indian Ocean basin mode and the impact on Asian summer

632 climate. *Geophysical Research Letters*, 46(21): 12388-12397.

633 Sun, B., Wang, H., Zhou, B. and Li, H., 2019b. Interdecadal variation in the synoptic features of mei-yu in the Yangtze

634 River valley region and relationship with the Pacific decadal oscillation. *Journal of Climate*, 32(19): 6251-6270.

635 Taylor, K.E., Stouffer, R.J. and Meehl, G.A., 2012. An overview of CMIP5 and the experiment design. *Bulletin of the*

636 *American Meteorological Society*, 93(4): 485-498.

637 Touma, D., Stevenson, S., Lehner, F. and Coats, S., 2021. Human-driven greenhouse gas and aerosol emissions cause

638 distinct regional impacts on extreme fire weather. *Nature Communications*, 12(1): 212.

639 Wang, B., Wu, Z., Li, J., Liu, J., Chang, C.-P., Ding, Y. and Wu, G., 2008. How to measure the strength of the East Asian

640 summer monsoon. *Journal of Climate*, 21(17): 4449-4463.

641 Wang, B., Xiang, B., Li, J., Webster, P.J., Rajeevan, M.N., Liu, J. and Ha, K.-J., 2015. Rethinking Indian monsoon rainfall

642 prediction in the context of recent global warming. *Nature Communications*, 6(1): 7154.

643 Wang, J., Zhu, Z.W., Qi, L., Zhao, Q.H., He, J.H. and Wang, J.X.L., 2019. Two pathways of how remote SST anomalies

644 drive the interannual variability of autumnal haze days in the Beijing–Tianjin–Hebei region, China. *Atmospheric*

645 *Chemistry and Physics*, 19(3): 1521-1535.

646 Wang, J., Liu, Y., Ding, Y. and Wu, Z., 2021. Towards influence of Arabian Sea SST anomalies on the withdrawal date of

647 Meiyu over the Yangtze-Huaihe River basin. *Atmospheric Research*, 249: 105340.

648 Wang, J., Liu, Y., Song, C., Ding, Y., Li, Q., Wu, P., Xu, Y. and Xu, X., 2022. Synergistic impacts of westerlies and

649 monsoon on interdecadal variations of late spring precipitation over the southeastern extension of the Tibetan

650 Plateau. *International Journal of Climatology*, 42(14): 7342-7361.

651 Wang, J., Liu, Y., Yang, Y., Wu, P., Yang, J., Liang, P., Song, C., Zhang, S. and Ding, Y., 2023. Impact of early winter

652 North Atlantic Oscillation on the dramatic alternation of seesaw haze intensity between late winter months in

653 the North China Plain. *Atmospheric Research*, 281: 106483.

654 Wang, L., Chen, W., Huang, G. and Zeng, G., 2017. Changes of the transitional climate zone in East Asia: past and future.

655 *Climate Dynamics*, 49(4): 1463-1477.

656 Wang, Q., Wang, L., Huang, G., Piao, J. and Chotamonsak, C., 2021. Temporal and spatial variation of the transitional

657 climate zone in summer during 1961–2018. *International Journal of Climatology*, 41(3): 1633-1648.

658 Wang, Q., Wang, L., Huang, G. and Wang, T., 2022. Mechanism of the summer rainfall interannual variability in

659 transitional climate zone in East Asia: roles of teleconnection patterns and associated moisture processes.

660 *Climate Dynamics*, <https://doi.org/10.1007/s00382-022-06618-1>.

661 Wang, Q., Huang, G., Wang, L., Piao, J., Ma, T., Hu, P., Chotamonsak, C. and Limsakul, A., 2023. Mechanism of the

662 summer rainfall variation in Transitional Climate Zone in East Asia from the perspective of moisture supply

663 during 1979–2010 based on the Lagrangian method. *Climate Dynamics*, 60(3): 1225-1238.

664 Wang, S., Huang, J., Huang, G., Luo, F., Ren, Y. and He, Y., 2022. Enhanced impacts of Indian Ocean sea surface

665 temperature on the dry/wet variations over Northwest China. *Journal of Geophysical Research: Atmospheres*,

666 127(11): e2022JD036533.

667 Wu, B., Zhou, T. and Li, T., 2016. Impacts of the Pacific–Japan and circumglobal teleconnection patterns on the

668 interdecadal variability of the East Asian summer monsoon. *Journal of Climate*, 29(9): 3253-3271.

669 Wu, G., Guan, Y., Liu, Y., Yan, J. and Mao, J., 2012. Air–sea interaction and formation of the Asian summer monsoon

670 onset vortex over the Bay of Bengal. *Climate Dynamics*, 38(1): 261-279.

671 Wu, P., Liu, Y., Ding, Y., Li, X. and Wang, J., 2022. Modulation of sea surface temperature over the North Atlantic and

672 Indian-Pacific warm pool on interdecadal change of summer precipitation over northwest China. *International*

673 *Journal of Climatology*, 42(16): 8526-8538.

674 Xie, S.-P., Hu, K., Hafner, J., Tokinaga, H., Du, Y., Huang, G. and Sampe, T., 2009. Indian Ocean capacitor effect on

675 Indo–western Pacific climate during the summer following El Niño. *Journal of Climate*, 22(3): 730-747.

676 Xing, W. and Wang, B., 2017. Predictability and prediction of summer rainfall in the arid and semi-arid regions of China.

677 *Climate Dynamics*, 49(1): 419-431.

678 Yang, D., Arblaster, J.M., Meehl, G.A., England, M.H., Lim, E.-P., Bates, S. and Rosenbloom, N., 2020. Role of tropical

679 variability in driving decadal shifts in the Southern Hemisphere summertime eddy-driven jet. *Journal of Climate*,

680 33(13): 5445-5463.

681 Yang, J., Liu, Q., Xie, S.-P., Liu, Z. and Wu, L., 2007. Impact of the Indian Ocean SST basin mode on the Asian summer

682 monsoon. *Geophysical Research Letters*, 34(2): L02708.

683 Yeh, T.-C., Dao, S.-Y. and Li, M.-T., 1959. The abrupt change of circulation over the Northern Hemisphere during June

684 and October. *The Atmosphere and the Sea in Motion*, the Rockefeller Institute Press and Oxford University Press,

685 249-267.

686 Ying, K., Jiang, D., Zheng, X., Frederiksen, C.S., Peng, J., Zhao, T. and Zhong, L., 2023. Seasonal predictable source of

687 the East Asian summer monsoon rainfall in addition to the ENSO–AO. *Climate Dynamics*, 60(7): 2459-2480.

688 You, Y. and Jia, X., 2018. Interannual variations and prediction of spring precipitation over China. *Journal of Climate*,

689 31(2): 655-670.

690 Zeng, J. and Zhang, Q., 2019. A humidity index for the summer monsoon transition zone in East Asia. *Climate Dynamics*,

691 53(9): 5511-5527.

692 Zhang, L., Han, W., Karnauskas, K.B., Meehl, G.A., Hu, A., Rosenbloom, N. and Shinoda, T., 2019. Indian Ocean

693 warming trend reduces Pacific warming response to anthropogenic greenhouse gases: An interbasin thermostat

694 mechanism. *Geophysical Research Letters*, 46(19): 10882-10890.

695 Zhang, Z., Sun, X. and Yang, X.-Q., 2018. Understanding the interdecadal variability of East Asian summer monsoon

696 precipitation: Joint influence of three oceanic signals. *Journal of Climate*, 31(14): 5485-5506.

697 Zhao, W., Chen, S., Chen, W., Yao, S., Nath, D. and Yu, B., 2019a. Interannual variations of the rainy season withdrawal

698 of the monsoon transitional zone in China. *Climate Dynamics*, 53(3): 2031-2046.

699 Zhao, W., Chen, W., Chen, S., Yao, S.-L. and Nath, D., 2019b. Inter-annual variations of precipitation over the monsoon

700 transitional zone in China during August–September: Role of sea surface temperature anomalies over the

701 tropical Pacific and North Atlantic. *Atmospheric Science Letters*, 20(1): e872.

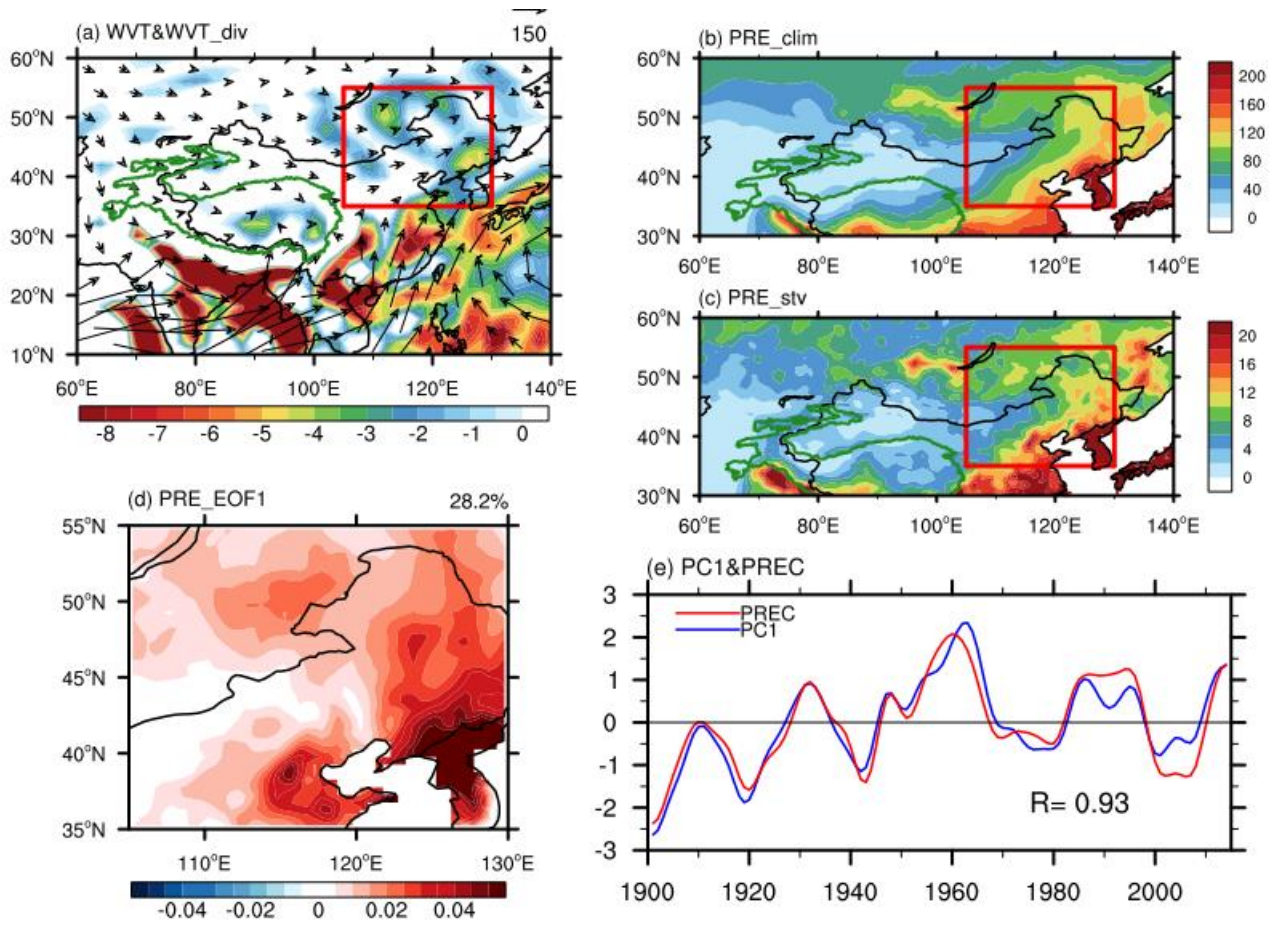
702 Zhao, W., Chen, W., Chen, S., Nath, D. and Wang, L., 2020. Interdecadal change in the impact of North Atlantic SST on

703 August rainfall over the monsoon transitional belt in China around the late 1990s. *Theoretical and Applied*

704 *Climatology*, 140(1): 503-516.

705
706
707
708
709
710
711
712
713
714
715
716
717
718
719
720
721
722
723
724

725 Figures
726



727

728 Figure 1. The climatological JJA-averaged (a) $\langle WVT \rangle$ (vectors; $\text{kg m}^{-1} \text{s}^{-1}$) and $\langle WVT_div \rangle$ (shading; $10^{-5} \text{ kg m}^{-2} \text{ s}^{-1}$), (b)
729 precipitation (mm month^{-1}), and (c) interdecadal standard deviation of precipitation (mm month^{-1}) during the period 1901–2014. The
730 red box (35° – 55°N , 105° – 130°E) outlines the research domain of EAMTZ (the same hereinafter). (d) Spatial pattern of the first
731 empirical orthogonal function (EOF1) mode of JJA-mean EAMTZ precipitation. (e) Normalized time series of the JJA-mean EAMTZ
732 precipitation index (I_{EAMTZP}) (red line) and associated first principal component (PC1) (blue line), with the number denoting the
733 temporal correlation coefficient (TCC) between the corresponding time series. In panels (c)–(e), variables are detrended and 11-year
734 low-pass filtered. The green outline in panels (a)–(c) represents the terrain of the Tibetan Plateau (TP) at 2000 m (the same hereinafter).
735 The precipitation is derived from the CRU TS3.26 precipitation data, while other variables are from the 20CRv2c datasets.

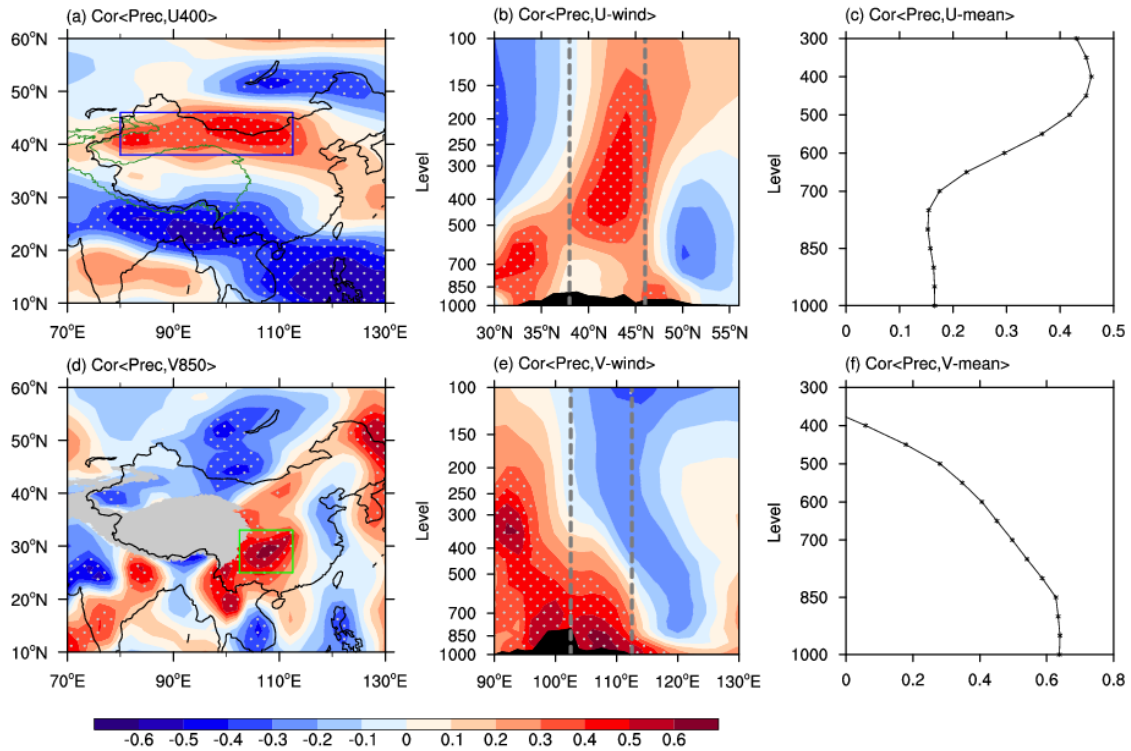
736

737

738

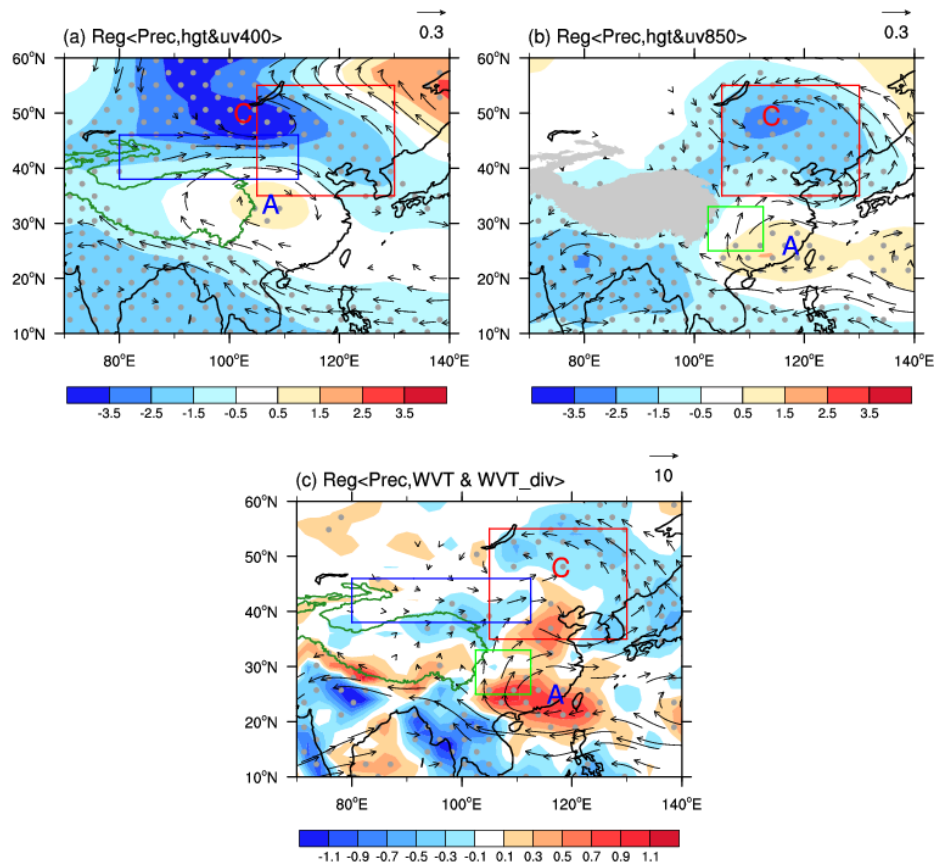
739

740



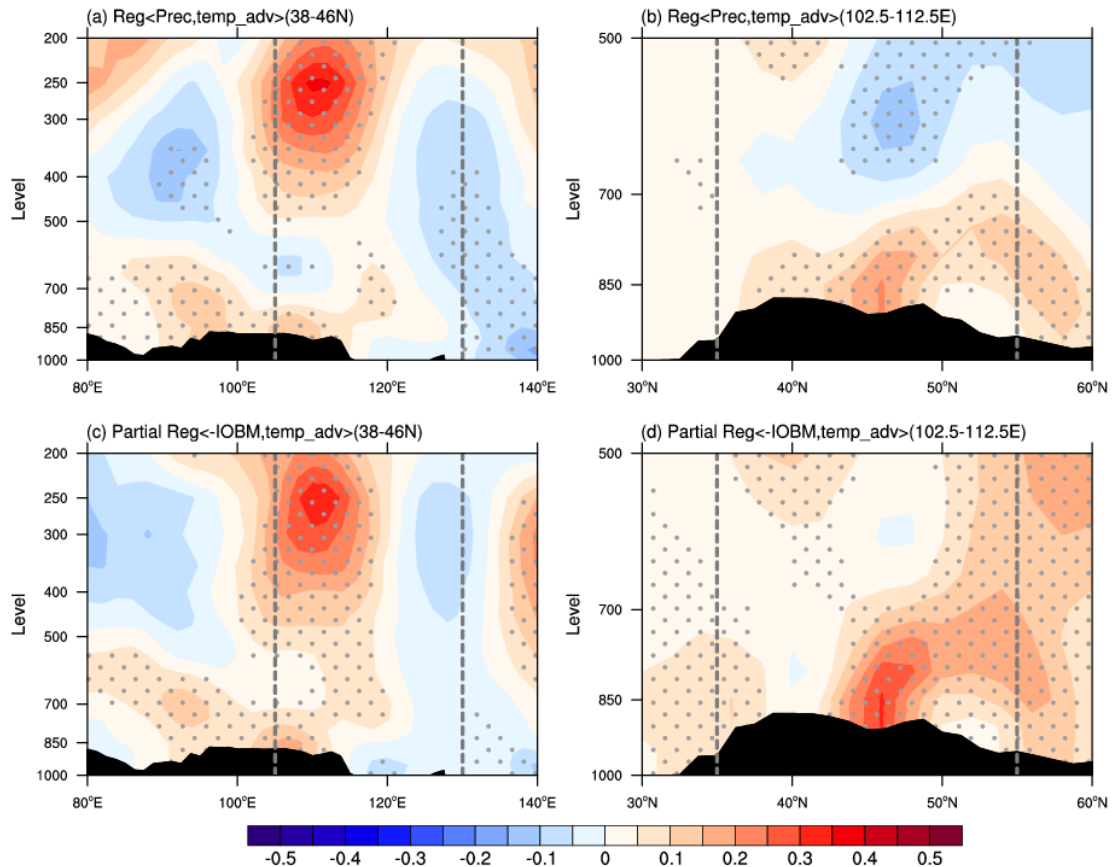
741
 742 Figure 2. Correlation maps of the JJA-averaged I_{EAMBZP} with the simultaneous (a) 400-hPa zonal wind and (d) 850-hPa meridional
 743 wind, and (b) height–latitude cross-section of zonal winds averaged over 80° – 112.5° E, and (e) height–longitude cross-section of
 744 meridional winds averaged over 25° – 33° N, during the period 1901–2014. The blue box (38° – 46° N, 80° – 112.5° E) in (a) and the green
 745 box (25° – 33° N, 102.5° – 112.5° E) in (d) represent the upstream westerly domain and the monsoonal southerly domain significantly tied
 746 to the interdecadal variations of precipitation over EAMBZ, respectively (the same hereinafter). The grey-dashed vertical lines in (b)
 747 and (e) represent the latitudinal and longitudinal range of the westerly and the monsoonal southerly domain, respectively. (c) Profile of
 748 correlation coefficients between the JJA-averaged I_{EAMBZP} and the simultaneous area-averaged zonal winds over the upstream westerly
 749 domain at multiple levels during the period 1901–2014. (f) As in (c), but for the meridional winds over the monsoonal southerly domain.
 750 All variables are detrended and 11-year low-pass filtered. Areas with significant values exceeding the 95% confidence level are stippled.
 751 The black shading indicates the topography. The grey shaded areas denote the TP areas above 2000 m (the same hereinafter). The
 752 I_{EAMBZP} is calculated based on the CRU TS3.26 precipitation data, while other variables are from the 20CRv2c datasets.

753
 754
 755
 756
 757
 758
 759
 760
 761
 762
 763



764
 765 Figure 3. Regression maps of the JJA-mean anomalies of (a) 400-hPa geopotential height (Z400; shading; m) and wind field (UV400;
 766 vectors; m s^{-1}), (b) 850-hPa geopotential height (Z850; shading; m) and wind field (UV850; vectors; m s^{-1}), and (c) $\langle \text{WVT} \rangle$ (vectors;
 767 $\text{kg m}^{-1} \text{s}^{-1}$) and $\langle \text{WVT}_{\text{div}} \rangle$ (shading; $10^{-5} \text{ kg m}^{-2} \text{s}^{-1}$) onto the concurrent I_{EAMBZP} during the period 1901–2014. All variables are
 768 detrended and 11-year low-pass filtered. Letter A (C) represents the center of anticyclonic (cyclonic) anomaly (the same hereinafter).
 769 Areas with significant values of Z400, Z850, and $\langle \text{WVT}_{\text{div}} \rangle$ that exceed the 95% confidence level are stippled, respectively. Only
 770 vectors that are significant at the 95% confidence level are shown. The I_{EAMBZP} is calculated based on the CRU TS3.26 precipitation
 771 data, while other variables are from the 20CRv2c datasets.

772
 773
 774
 775
 776
 777
 778
 779
 780
 781
 782
 783
 784



785

786

787

788

789

790

791

792

793

794

795

796

797

798

799

800

801

802

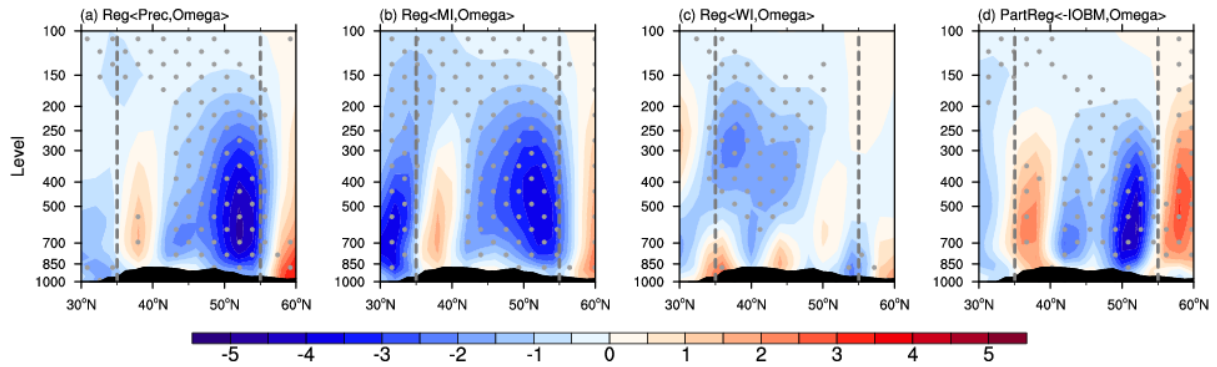
803

804

805

806

Figure 4. (a) Height–longitude cross-section (averaged over 38°–46°N) and (b) height–latitude cross-section (averaged over 102.5°–112.5°E) of the JJA-mean temperature advection anomalies (shading; 10^{-5} K s^{-1}) regressed onto the concurrent I_{EAMBZP} during the period 1901–2014. (c, d) As in (a, b), but for patterns of the partial regression coefficient between temperature advection and negative I_{IOBM} without the IPO ~~signal~~ forcing. The gray vertical lines in (a, c) and (b, d) represent the longitudinal and latitudinal range of the research domain of EAMBZ, respectively. The black shading indicates the topography. All variables are detrended and 11-year low-pass filtered. Areas with significant values exceeding the 95% confidence level are stippled. The I_{EAMBZP} and I_{IOBM} /IPO index are calculated based on the CRU TS3.26 precipitation data and the ERSSTv5 dataset, respectively; whilst other variables are from the 20CRv2c datasets.



807

808

809

810

811

812

813

814

815

816

817

818

819

820

821

822

823

824

825

826

827

828

829

830

831

832

833

834

835

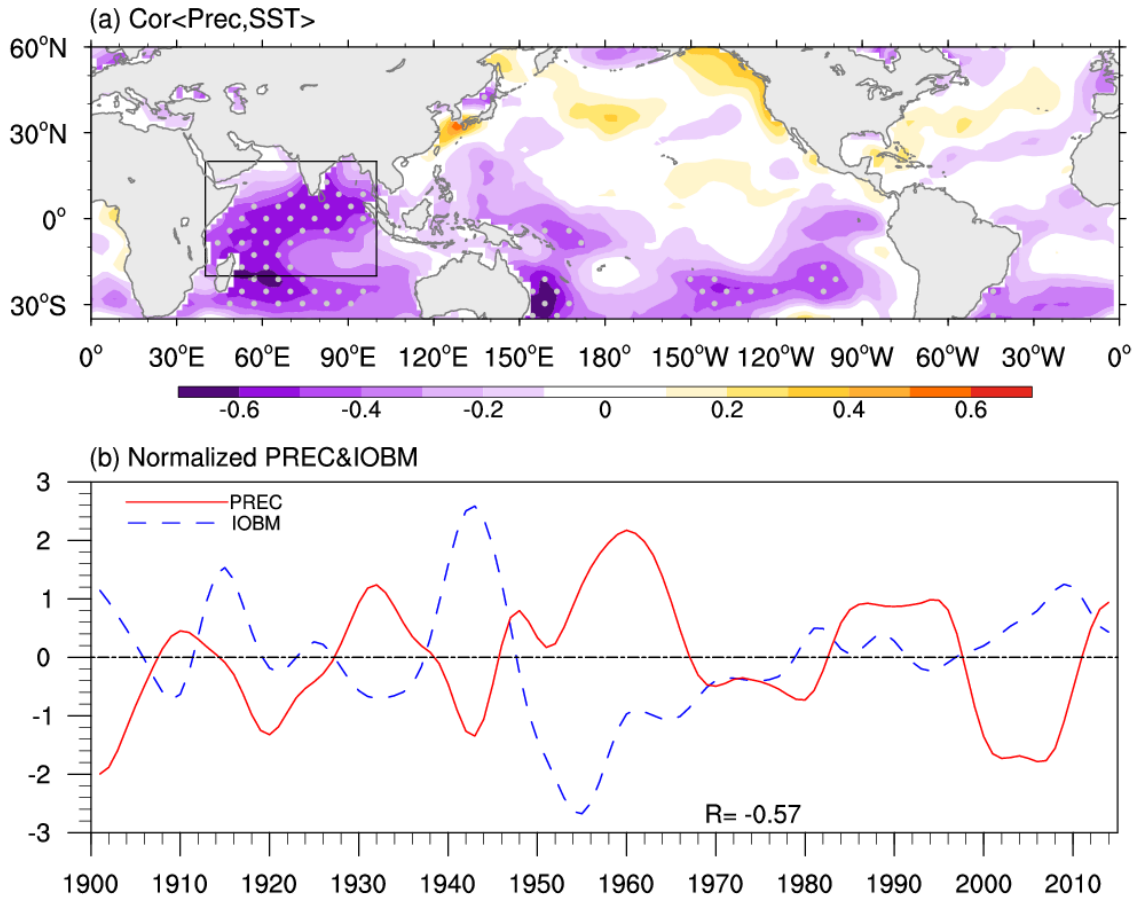
836

837

838

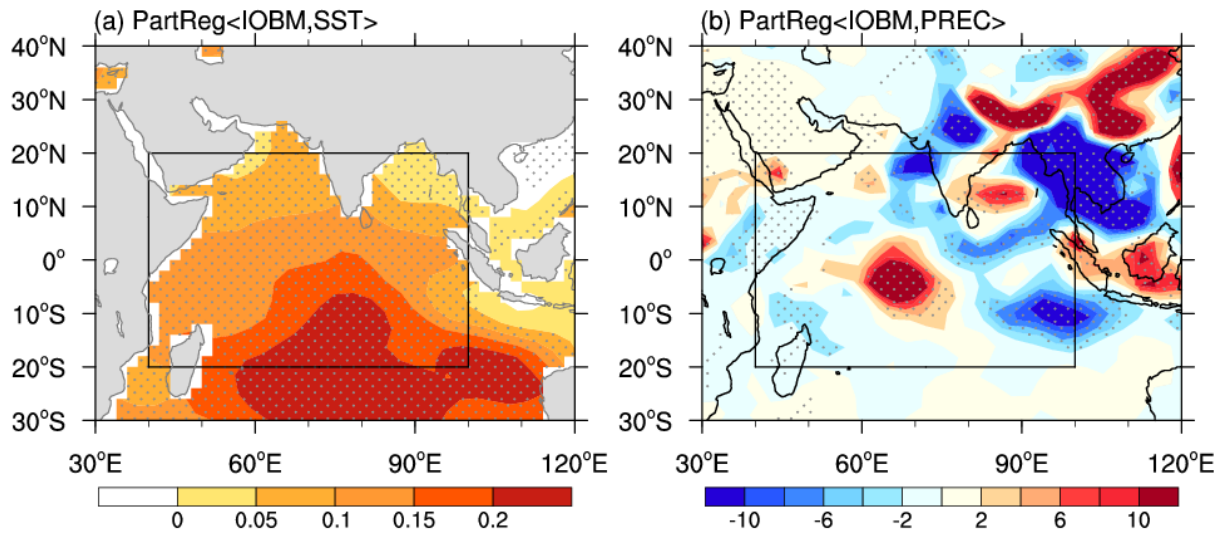
839

Figure 5. Height–latitude cross-section (averaged over 105°–130°E) of the JJA-mean vertical velocity anomalies ($10^{-3} \text{ Pa s}^{-1}$) regressed onto the concurrent (a) I_{EAMBZP} , (b) I_{MI} , and (c) I_{WI} during the period 1901–2014. (d) As in (a), but for the partial regressed anomalies onto the negative I_{IOBM} with the IPO [signal forcing](#) removed. The gray vertical lines represent the latitudinal range of EAMBZ. The black shading indicates the topography. All variables are detrended and 11-year low-pass filtered. Areas with significant values exceeding the 95% confidence level are stippled. The I_{EAMBZP} and $I_{\text{IOBM/IPO}}$ index are calculated based on the CRU TS3.26 precipitation data and the ERSSTv5 dataset, respectively; whilst other variables are from the 20CRv2c datasets.



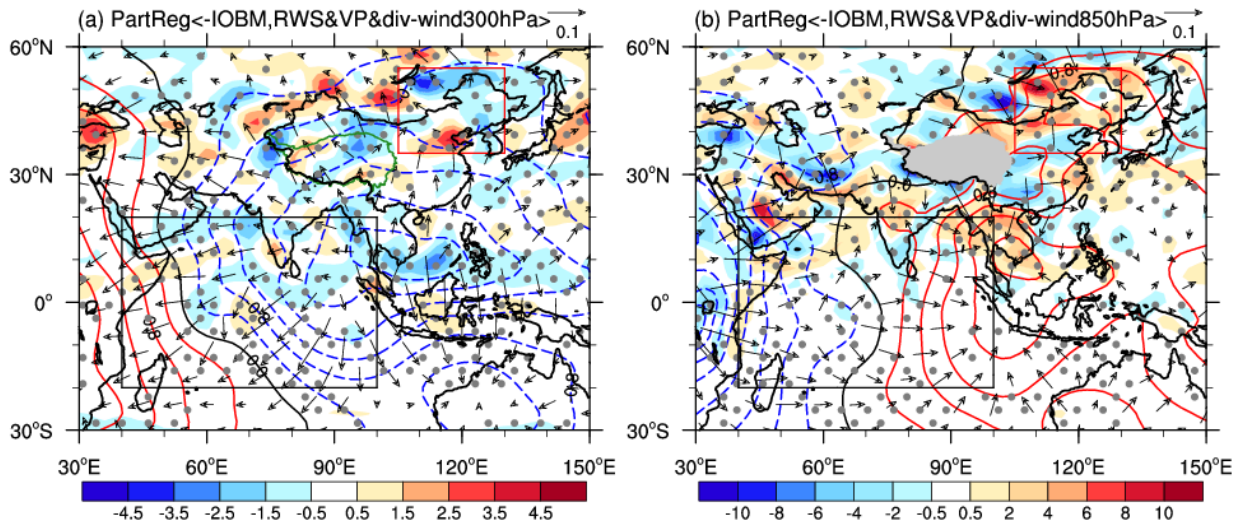
840
 841 Figure 6. (a) Correlation map of the JJA-mean I_{EAMBZP} with the concurrent near-global SST (35°S – 60°N) during the period 1901–2014.
 842 The black frame (20°S – 20°N , 40° – 100°E) outlines the domain for delineating the IOBM mode (the same hereinafter). Areas with
 843 significant values exceeding the 99% confidence level are stippled. (b) Normalized time series of the JJA-mean I_{EAMBZP} (red line) and
 844 I_{IOBM} (blue line) from 1901 to 2014. The numeral at the bottom represents the TCC between the corresponding time series. All variables
 845 are detrended and 11-year low-pass filtered. The SST is from the ERSSTv5 dataset. The I_{EAMBZP} and I_{IOBM} are calculated based on the
 846 CRU TS3.26 precipitation data and the ERSSTv5 datasets, respectively.

847
 848
 849
 850
 851
 852
 853
 854
 855
 856
 857
 858
 859



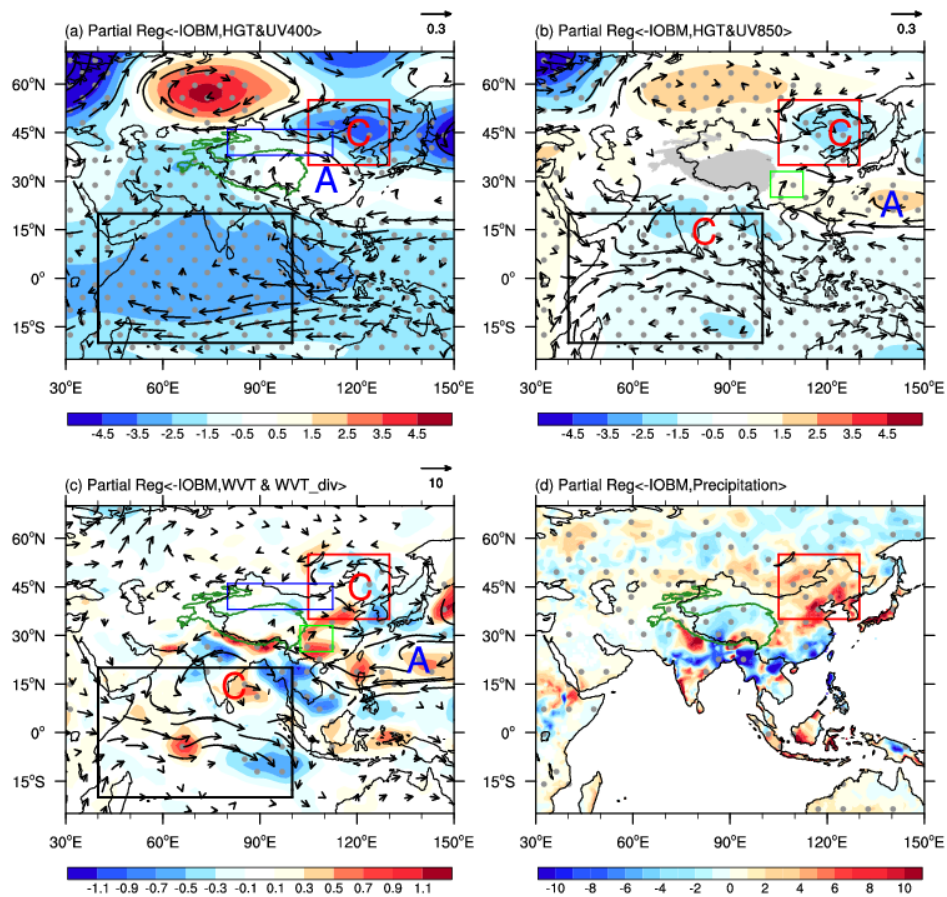
860
 861 Figure 7. Partial regression of the JJA-mean (a) SST (°C) and (b) precipitation (mm month⁻¹) anomalies over TIO and its neighboring
 862 areas onto the concurrent I_{IOBM} with the IPO signal-forcing removed for the period 1901–2014. All variables are detrended and 11-year
 863 low-pass filtered. Areas with significant values exceeding the 95% confidence level are stippled. The I_{IOBM} /IPO index is calculated
 864 based on the ERSSTv5 dataset. The SST and the precipitation are derived from the ERSSTv5 dataset and the 20CRv2c dataset,
 865 respectively.

866
 867
 868
 869
 870
 871
 872
 873
 874
 875
 876
 877
 878
 879
 880
 881
 882



883
 884 Figure 8. Partial regression of the JJA-mean (a) 300- and (b) 850-hPa RWS (shading; 10^{-11} s^{-2}), velocity potential (contours; interval:
 885 $0.4; 10^5 \text{ m}^2 \text{ s}^{-1}$), and divergent horizontal wind (vectors; m s^{-1}) anomalies against the concurrent negative I_{IOBM} with the IPO **signal**
 886 **forcing** removed during the period 1901–2014. All variables are detrended and 11-year low-pass filtered. Areas with significant values
 887 of RWS exceeding the 95% confidence level are stippled. The I_{IOBM} /IPO index is calculated based on the ERSSTv5 dataset; whilst
 888 other variables are from the 20CRv2c datasets.

889
 890
 891
 892
 893
 894
 895
 896
 897
 898
 899
 900
 901
 902
 903
 904
 905
 906
 907
 908
 909
 910
 911
 912
 913
 914



915

916

917

918

919

920

921

922

923

924

925

926

927

928

929

930

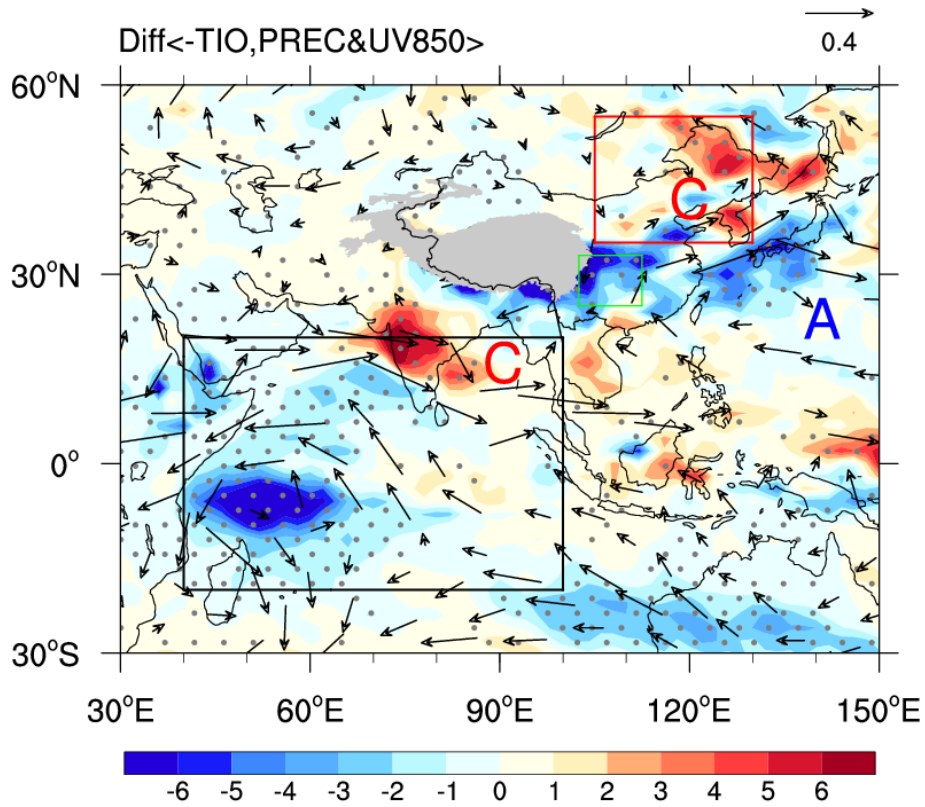
931

932

933

934

Figure 9. Partial regression of the JJA-mean (a) Z400 (shading; m) and UV400 (vectors; m s^{-1}), (b) Z850 (shading; m) and UV850 (vectors; m s^{-1}), (c) $\langle \text{WVT} \rangle$ (vectors; $\text{kg m}^{-1} \text{ s}^{-1}$) and $\langle \text{WVT}_{\text{div}} \rangle$ (shading; $10^{-5} \text{ kg m}^{-2} \text{ s}^{-1}$), and precipitation (mm month^{-1}) anomalies onto the concurrent negative I_{OIBM} with the IPO signal-forcing removed during the period 1901–2014. All variables are detrended and 11-year low-pass filtered. Areas with significant values of Z400, Z850, and $\langle \text{WVT}_{\text{div}} \rangle$ that exceed the 95% confidence level are stippled, respectively. Only vectors that are significant at the 95% confidence level are shown. The I_{OIBM} /IPO index is calculated based on the ERSSTv5 dataset; the precipitation is derived from the CRU TS3.26 precipitation data; whilst other variables are from the 20CRv2c datasets.



935

936

937

938

939

940

941

942

943

944

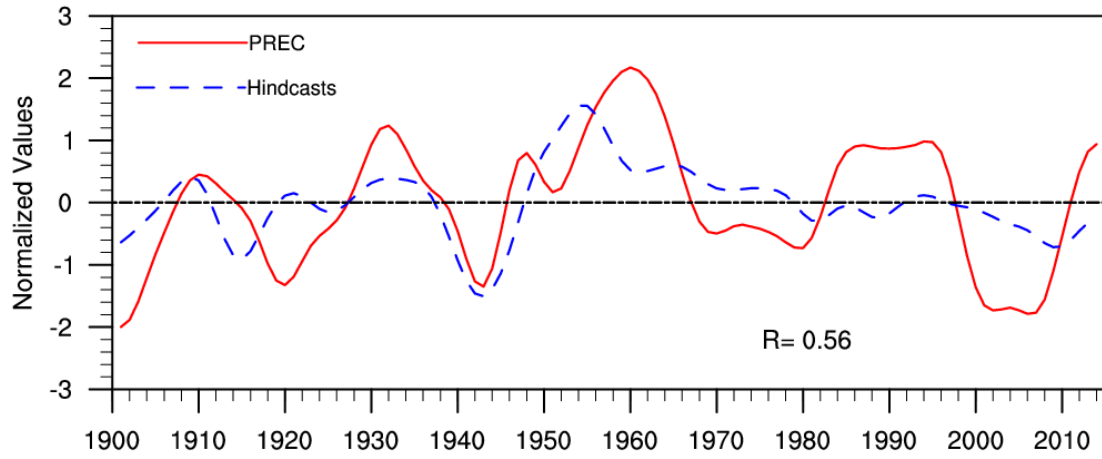
945

946

947

948

Figure 10. Simulated composite differences of JJA-mean UV850 (vectors; m s^{-1}) and precipitation (shading; mm month^{-1}) between cold and warm SST years over the broader TIO domain in CESM1_IOPES (15°S – 15°N , 40° – 174°E ; purple box in Fig. S4). The warm and cold TIO SST years are selected based on the ± 0.5 standard deviations of the simulated time-evolving SSTAs during 1920–2005, as shown in Fig. S3 (red line). All variables are detrended and 11-year low-pass filtered. Areas with significant values of precipitation that exceed the 95% confidence level are stippled. Only vectors that are significant at the 95% confidence level are shown. The simulated anomalies of UV850 and precipitation are calculated based on the difference between the CESM1_IOPES ensemble mean and the CESM1_LENS ensemble mean (former minus latter), highlighting the internally driven impacts of TIO SSTAs.



949

950

Figure 11. Normalized time series of the JJA-mean I_{EAMBZP} (red line) and associated leave-one-out cross-validated hindcast estimates (blue line) for 1901–2014, with the number denoting the TCC between the corresponding time series.

951

952

953

954

955

956

957

958

959

960

961

962

963

964

965

966

967

968

969

970

971

972

973

974

975

976

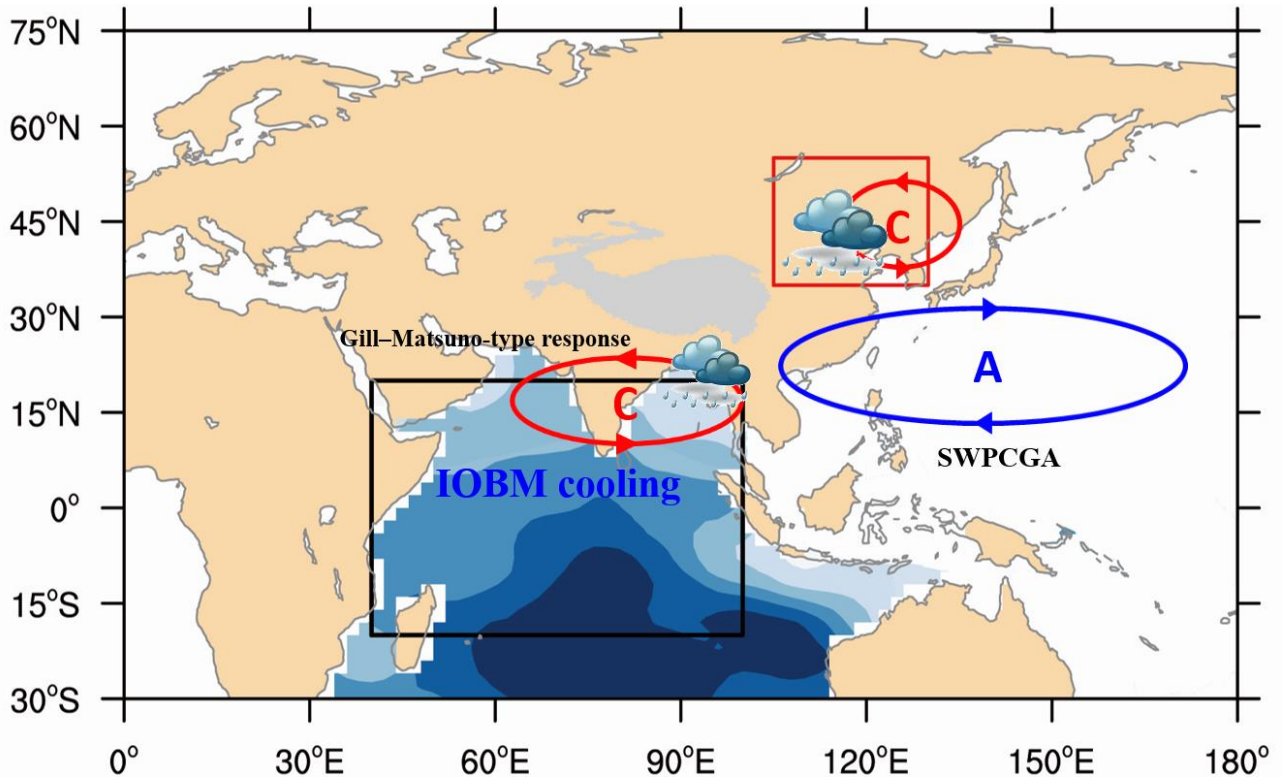
977

978

979

980

981



982

983

984

985

986

987

988

989

Figure 12. Schematic diagram showing how IOBM-related SST anomaly pattern drives the summer EAM/BZ precipitation fluctuations at interdecadal timescales. Blue shading illustrates the IOBM cooling. Letter A (C) indicates the center of the anticyclonic (cyclonic) gyre anomaly.